

Table of Contents

Table of Contents	1
List of Figures	2
1 Glossary	3
2 Results	1
2.1 Description of Runs	1
2.2 Relevant Definitions	2
2.3 Verifying the Model Output	4
2.3.1 Time till well-mixed	4
2.3.2 FFT Energy Spectra	8
2.3.3 Ensemble and horizontally averaged vertical Potential Temperature $\bar{\theta}$ and Heat Flux profiles $\overline{w'\theta'}$	10
2.3.4 Visualization of Structures Within the Entrainment Layer	12
2.4 Local Mixed Layer Heights (h_0^l)	15
2.5 Flux Quadrants	20
2.6 h and Δh based on Average Profiles	25
2.6.1 Reminder of Relevant Definitions	25
2.6.2 $\frac{w_e}{w^*}$ vs Ri^{-1}	27
2.6.3 $\frac{\Delta h}{h}$ vs Ri^{-1}	30
3 discussion	37
3.1 Description of Runs	37

3.2	Relevant Definitions	38
3.3	Verifying the Model Output	41
3.3.1	Time till well-mixed	41
3.3.2	FFT Energy Spectra	42
3.3.3	Ensemble and horizontally averaged vertical Potential Temperature $\bar{\theta}$ and Heat Flux profiles $\overline{w'\theta'}$	42
3.3.4	Visualization of Structures within the Entrainment Layer	43
3.4	Local Mixed Layer Heights (h_0^l)	44
3.5	Flux Quadrants	46
3.6	h and Δh based on Average Profiles	47
3.6.1	Reminder of Relevant Definitions	47
3.6.2	$\frac{w_e}{w^*}$ vs Ri^{-1}	47
3.6.3	$\frac{\Delta h}{h}$ vs Ri^{-1}	48
Bibliography		51

List of Figures

Figure 2.1	Height Definitions	3
Figure 2.2	Plots of scaled time vs time for all runs. Scaled time is based on the convective time scale and can be thought of as the number of times an eddie has reached the top of the CBL.	5
Figure 2.3	Vertical profiles of the ensemble and horizontally averaged potential temperature ($\bar{\theta}$), its vertical gradient ($\frac{\partial \bar{\theta}}{\partial z}$) and heat flux ($\overline{w'\theta'}$) for the 150/10 run	6
Figure 2.4	$\overline{w'\theta'}$ and scaled $\overline{w'\theta'}$ vs scaled height for the 150/10 run .	6
Figure 2.5	$\sqrt{w'^2}$ vs scaled height for the 150/10 run	7
Figure 2.6	Scalar FFT energy vs wavenumber ($k = \sqrt{k_x^2 + k_y^2}$) for the 60/2.5 run at 2 hours. $E(k)$ is $E(k_x, k_y)$ integrated around circles of radius k . $E(k_x, k_y)$ is the total integrated energy over the 2D domain. k_x and k_y are number of waves per domain length.	9
Figure 2.7	$\bar{\theta}$ profiles at 2 hours	10
Figure 2.8	Scaled $\overline{w'\theta'}_s$ profiles at 2 hours	11
Figure 2.9	θ' (left) and w' (right) at 2 hours at h_0 (a,d), h (c,e) and h_1 (d,f)	13
Figure 2.10	θ' (left) and w' (right) at 2 hours at h_0 (a,d), h (b,e) and h_1 (c,f)	14
Figure 2.11	Local vertical θ profiles with 3-line fit for the 60/2.5 (a) and 150/10 (b) runs at points where h_0^l is high.	16

Figure 2.12	Local vertical θ profiles with 3-line fit for the 60/2.5 (a) and 150/10 (b) runs at points where h_0^l is low.	16
Figure 2.13	θ' (a,d), w' (b,e) at h_1 (c,f) and local ML height h_0^l at 2 hours for 60/2.5 (left) and 150/10 (right) runs	17
Figure 2.14	Histograms of h_0^l for $\overline{w'\theta'_s} = 150$ to $60(W/m^2)$ (a to c) and $\gamma = 10$ to $2.5(K/Km)$ (c to g) at 5 hours	18
Figure 2.15	PDFs of $\frac{h_0^l}{h}$ for $\overline{w'\theta'_s} = 150$ to $60(W/m^2)$ (a to c) and $\gamma = 10$ to $2.5(K/Km)$ (c to g) at 5 hours	19
Figure 2.16	Scaled $\overline{w'\theta'}$ quadrant profiles at 5 hours for the 60/2.5 (a) and 150/10 (b) run	21
Figure 2.17	$\overline{w'\theta'}$ quadrants at h_0 for $w'\theta' = 150 - 60(W/m^2)$ (top- bottom) and $\gamma = 10 - 2.5(K/Km)$ (left-right) at 5 hours	22
Figure 2.18	$\overline{w'\theta'}$ quadrants at h for $w'\theta' = 150 - 60(W/m^2)$ (top - bottom) and $\gamma = 10 - 2.5(K/Km)$ (left - right) at 5 hours	23
Figure 2.19	$\overline{w'\theta'}$ quadrants at h_1 for $w'\theta' = 150$ to $60(W/m^2)$ (top to bottom) and $\gamma = 10$ to $2.5(K/Km)$ (left to right) at 5 hours	24
Figure 2.20	Height Definitions	25
Figure 2.21	h vs time for all runs	27
Figure 2.22	Log-Log plot of h vs time for all runs	28
Figure 2.23	$\frac{z_f}{h}$ vs Time	28
Figure 2.24	Inverse bulk Richardson Number vs time	29
Figure 2.25	Scaled Entrainment rate vs inverse Richardson Number (Ri)	29
Figure 2.26	Scaled Entrainment Layer limits ($\frac{h_1}{h}$ and $\frac{h_0}{h}$) vs time	31
Figure 2.27	Scaled Entrainment Layer limits (z_{f1} and z_{f0}) vs time	31
Figure 2.28	Vertical $\frac{\partial \bar{\theta}}{\partial z}$ profiles with threshold at .0002	32
Figure 2.29	Scaled EL depth vs inverse bulk Richardson Number with threshold at .0002	32
Figure 2.30	Vertical $\frac{\partial \bar{\theta}}{\partial z}$ profiles with threshold at .0004	33
Figure 2.31	Scaled EL depth vs inverse Richardson Number with thresh- old at .0004	33
Figure 2.32	Vertical $\frac{\partial \bar{\theta}}{\partial z}$ profiles with threshold at .0001	34

Figure 2.33	Scaled EL depth vs inverse bulk Richardson Number with threshold at .0001	34
Figure 2.34	Scaled vertical $\frac{\partial \bar{\theta}}{\partial z}$ profiles with threshold at .03	35
Figure 2.35	Revised height definitions based on scaled $\frac{\partial \bar{\theta}}{\partial z}$ profiles with threshold at .03	35
Figure 2.36	Scaled EL Depths vs inverse bulk Richardson number based on scaled $\frac{\partial \bar{\theta}}{\partial z}$ (a) and $\frac{\partial \bar{\theta}}{\partial z}$ (b)	36
Figure 2.37	Scaled Entrainment Rate vs inverse bulk Richardson num- ber based on scaled $\frac{\partial \bar{\theta}}{\partial z}$ (a) and $\frac{\partial \bar{\theta}}{\partial z}$ (b)	36

Chapter 1

Glossary

EL Entrainment Layer

ML Mixed Layer

CBL Convective Boundary Layer

LES Large Eddy Simulation

FFT Fast Fourier Transform

Ri Richardson Number , the bulk Richardson Number is $\frac{gh}{\bar{\theta}_{ML}} \frac{\Delta\theta}{w^{*2}}$, $\Delta\theta = \bar{\theta}(h_1) - \bar{\theta}(h_0)$

Chapter 2

Results

2.1 Description of Runs

All 10 member cases of the ensemble were carried out on a 3.2 x 4.8 Km horizontal domain ($\Delta x = \Delta y = 25m$, $nx = 128$, $ny = 192$). nx , ny were chosen based on the optimal distribution accross processor nodes. The vertical grid ($nz = 312$) was of higher resolution around the entrainment layer (EL) ($\Delta z = 5m$), and lower below and above it ($\Delta z = 10$ to $100m$). Grid size was chosen so that a full spectrum of turbulence would be resolved within the EL in line with the findings of Sullivan and Patton in [13]. The 7 runs vary depending on surface heat flux ($\overline{w'\theta'_s}$) and initial lapse rate (γ).

$\overline{w'\theta'_s} / \gamma$	10 (K/Km)	5 (K/Km)	2.5 (K/Km)
150 (W/m2)	✓	✓ ¹	
100 (W/m2)	✓	✓	
60 (W/m2)	✓	✓	✓

Table 2.1: Runs in terms of $\overline{w'\theta'_s}$ and initial lapse rate γ

¹Incomplete run: EL exceded high resolution vertical grid after 7 hours

2.2 Relevant Definitions

In large eddy simulation (LES) studies, the CBL height is usually defined as either the point of minimum $\overline{w'\theta'}$ or maximum $\frac{\partial\bar{\theta}}{\partial z}$. A notable exception is the work of Brooks and Fowler in [2] where the authors favoured a statistically based definition using local tracer profiles. Similarly, they define the entrainment layer (EL) in terms of the statistics of local profiles, whereas elsewhere in the literature it is usually defined according to the zero crossings in the vertical $\overline{w'\theta'}$ profile.

Here, the CBL height and EL limits are defined based on the vertical $\frac{\partial\bar{\theta}}{\partial z}$ profile. Namely, the CBL height h is the point where $\frac{\partial\bar{\theta}}{\partial z}$ is maximum, the lower EL limit is the point at which $\frac{\partial\bar{\theta}}{\partial z}$ first increases significantly from zero i.e. exceeds a threshold value above the surface layer, and the upper EL limit h_1 is the point where $\frac{\partial\bar{\theta}}{\partial z}$ resumes γ . (Figure 2.1)

As Brooks and Fowler point out in [2], when using an average vertical tracer profile there is no universal critereon for a significant gradient. So a threshold value for the lower EL limit (h_0) was chosen such that it was positive, small i.e. an order of magnitude less than γ and the same for all runs. For the sake of rigor, the main corresponding result was calculated based on two additional threshold values in Section 3.6.3.

The temperature jump is defined here as the difference in $\bar{\theta}$ accross the EL. So, it is larger than those used by Federovich et al. in [4] to verify their zero order model and Sullivan et al. in [14] (Table 2.2).

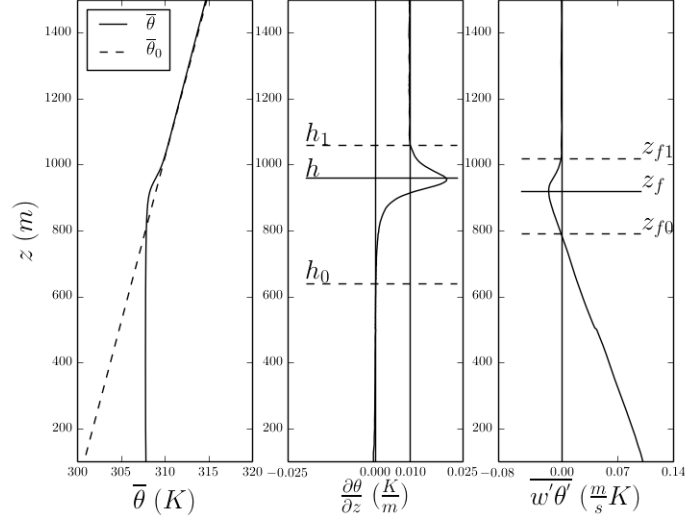


Figure 2.1: Height Definitions

Description	This Study	Sullivan et al. [14]	Fedorovich et al.[4]
CBL Height	\bar{h}_l	h	z_f
Temperature Jump	$\Delta\theta = \bar{\theta}(h_1) - \bar{\theta}(h_0)$	$\Delta\theta = \bar{\theta}(z_{f1}) - \bar{\theta}(z_f)$	$\Delta b = b_0(z_f) - b(z_{f0})$
			$\delta b = b(z_{f1}) - b(z_{f0})$
Convective Velocity Scale	$w_* = \frac{(hB_s)^{\frac{1}{3}}}{B_s} = \frac{g}{\theta_{ML}} \bar{w}'\theta'_s$	$w_* = \frac{(hB_s)^{\frac{1}{3}}}{B_s} = \frac{g}{\theta_{ML}} \bar{w}'\theta'_s$	$w_* = (z_f B_s)^{\frac{1}{3}}$
Time Scale	$\tau = \frac{h}{w_*}$	$\tau = \frac{h}{w_*}$	$\tau = N^{-1}$

Table 2.2: Comparison of relevant definitions with those from key publications. $b = \frac{g}{\theta_{ML}} \bar{\theta}$

2.3 Verifying the Model Output

2.3.1 Time till well-mixed

Time must be allowed to establish statistically steady turbulent flow. Sullivan et al. in [14] recommended 10 eddy turnover times based on the convective time scale $\tau = \frac{h}{w^*} = \frac{h}{\left(\frac{gh}{\bar{\theta}_{ML}} \overline{(w'\theta'_s)}\right)^{\frac{1}{3}}}$, and Brooks and Fowler in [2] chose a simulated time of 2 hours. For all of the runs, at least 10 eddy turnover times were completed by 2 simulated hours (Figure 2.2). Although each run has a distinct convective velocity scale that increases with time ($w^*(time)$), dividing boundary layer height (h) by it to obtain τ results in a collapse from 7 to 3 curves, one for each γ .

A measureable well mixed layer (ML) and EL based on the horizontally averaged, ensemble averaged potential temperature ($\bar{\theta}$) profile develops after 2 hours (Figure 2.3). After 2 or 3 hours the EL is fully contained within the vertical region of high resolution.

Averaged heat fluxes ($\overline{(w'\theta')}$) (Figure 2.4) and root mean squared vertical velocity perturbations ($\sqrt{\overline{w'^2}}$) (Figure 2.5) become self similar and are scaled well by the surface heat flux ($\overline{(w'\theta'_s)}$) and the convective velocity scale (w^*) respectively after 2 hours.

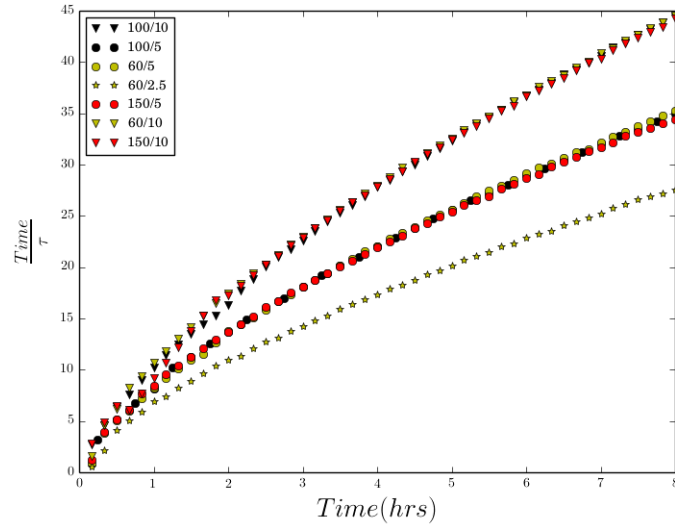


Figure 2.2: Plots of scaled time vs time for all runs. Scaled time is based on the convective time scale and can be thought of as the number of times an eddie has reached the top of the CBL.

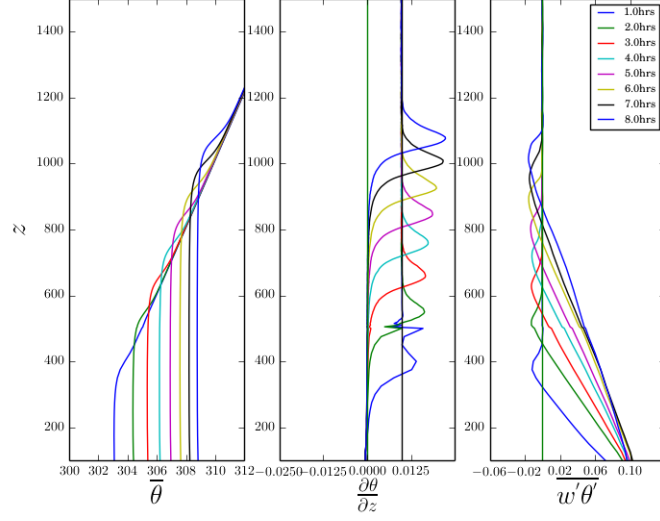


Figure 2.3: Vertical profiles of the ensemble and horizontally averaged potential temperature ($\bar{\theta}$), its vertical gradient ($\frac{\partial \bar{\theta}}{\partial z}$) and heat flux ($\overline{w'\theta'}$) for the 150/10 run

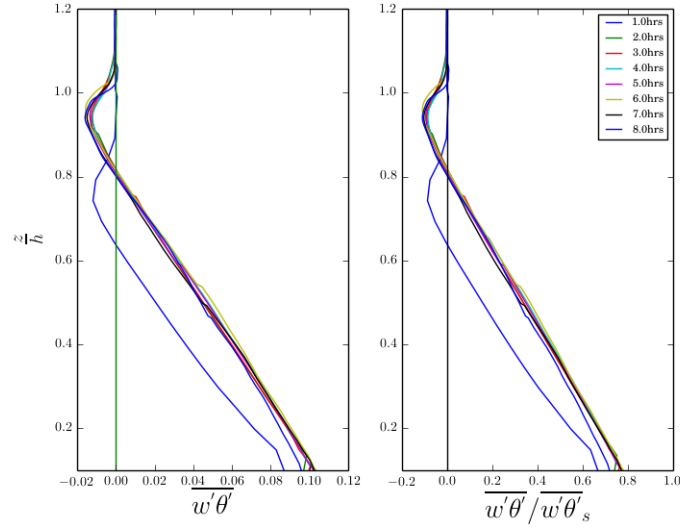


Figure 2.4: $\overline{w'\theta'}$ and scaled $\overline{w'\theta'}$ vs scaled height for the 150/10 run

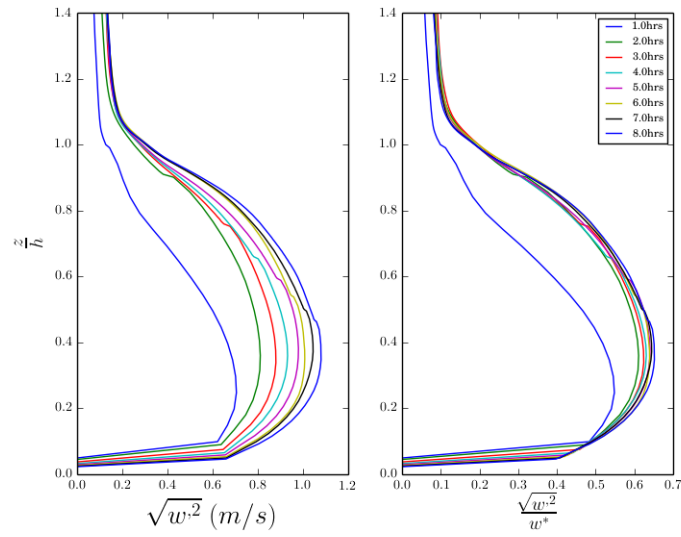


Figure 2.5: $\sqrt{w'^2}$ vs scaled height for the 150/10 run

2.3.2 FFT Energy Spectra

Two dimensional FFT power spectra taken of horizontal slices of w' (Figure 2.6) at three different levels (h_0 , h and h_1) are collapsed to one dimension by integrating around a circle of wave-number radius k . Isotropy in all radial directions is assumed and $k = \sqrt{k_x^2 + k_y^2}$.

The resulting scalar density spectra show peaks in energy at the larger scales, cascading to the lower scales roughly according to a $\frac{-5}{3}$ slope, lower in the EL. At the top of the EL where turbulence is suppressed by stability, the slope is steeper. The peak in energy occurs at smaller scales at the inversion (h) as compared to at the bottom of the EL (h_0), indicating a change in the size of the dominant turbulent structures further into the entrainment layer (EL).

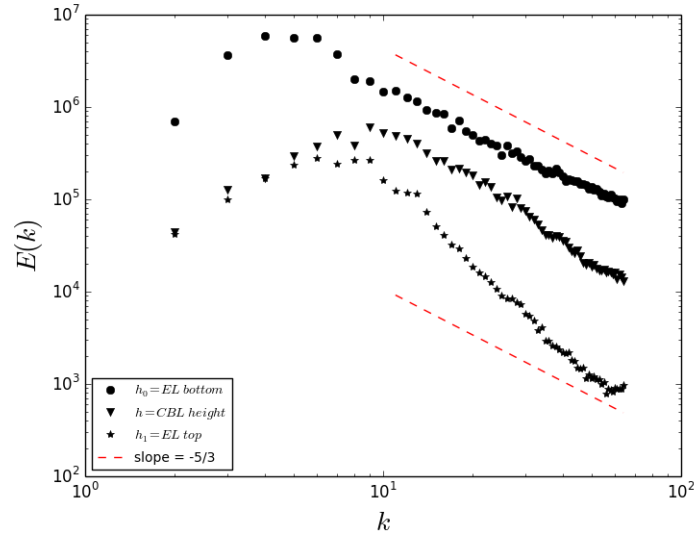


Figure 2.6: Scalar FFT energy vs wavenumber ($k = \sqrt{k_x^2 + k_y^2}$) for the 60/2.5 run at 2 hours. $E(k)$ is $E(k_x, k_y)$ integrated around circles of radius k . $E(k_x, k_y)$ is the total integrated energy over the 2D domain. k_x and k_y are number of waves per domain length.

2.3.3 Ensemble and horizontally averaged vertical Potential Temperature $\bar{\theta}$ and Heat Flux profiles $\overline{w'\theta'}$

The $\bar{\theta}$ profiles exhibit an ML above which $\frac{\partial \bar{\theta}}{\partial z} > 0$ and reaches a maximum value at h before resuming γ at h_1 (Figures 2.3 and 2.7). Convective boundary layer CBL growth is stimulated by $\overline{w'\theta'_s}$ and inhibited by γ .

The horizontally averaged, ensemble averaged heat flux ($\overline{w'\theta'}$) profiles decrease from the surface value ($\overline{w'\theta'_s}$) passing through zero to a minimum before increasing to zero (Figures 2.3 and 2.8). All minima are less in magnitude than the zero order approximation ($-.2 \times \overline{w'\theta'_s}$).

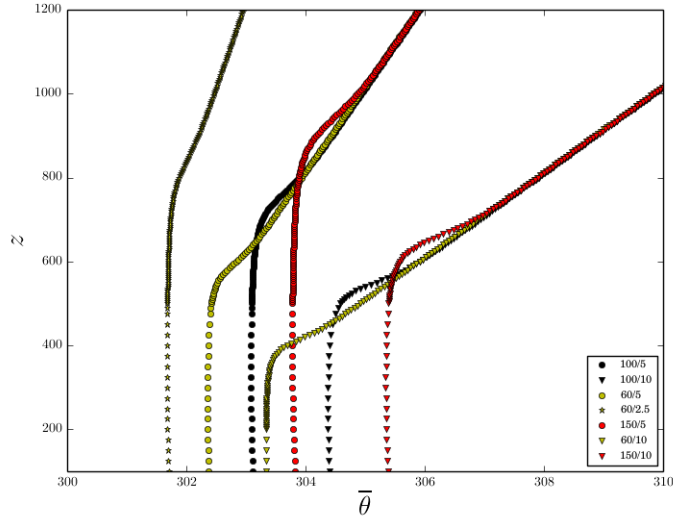


Figure 2.7: $\bar{\theta}$ profiles at 2 hours

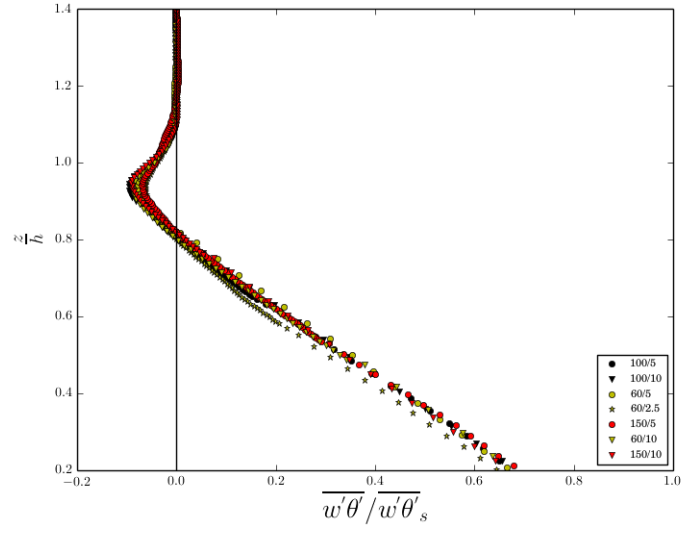


Figure 2.8: Scaled $\overline{w'\theta'_s}$ profiles at 2 hours

2.3.4 Visualization of Structures Within the Entrainment Layer

Horizontal slices, at the three entrainment layer (EL) levels, of the potential temperature and vertical velocity perturbations are plotted to see the turbulent structures. At the bottom of the EL (h_0) in the 150/10 run (Figure 2.9 (a) and (d)) coherent areas of positive and negative temperature perturbations correspond to areas of upward and downward moving air.

The individual plumes of relatively cool air are more evident at the inversion (h) and their locations correspond to areas of upward motion ((b) and (e)). Most of the upward moving cool areas are adjacent to and even encircled by smaller areas of downward moving warm air. At h_1 ((c) and (f)) peaks of cool air are associated with both up and down-welling.

In the 60/2.5 run (Figure 2.10) a similar progression is evident but the impinging, cool upward moving plumes are more defined. This is to be expected since stronger stability inhibits deformation of the inversion interface.

Figure 2.9: θ' (left) and w' (right) at 2 hours at h_0 (a,d), h (c,e) and h_1 (d,f)

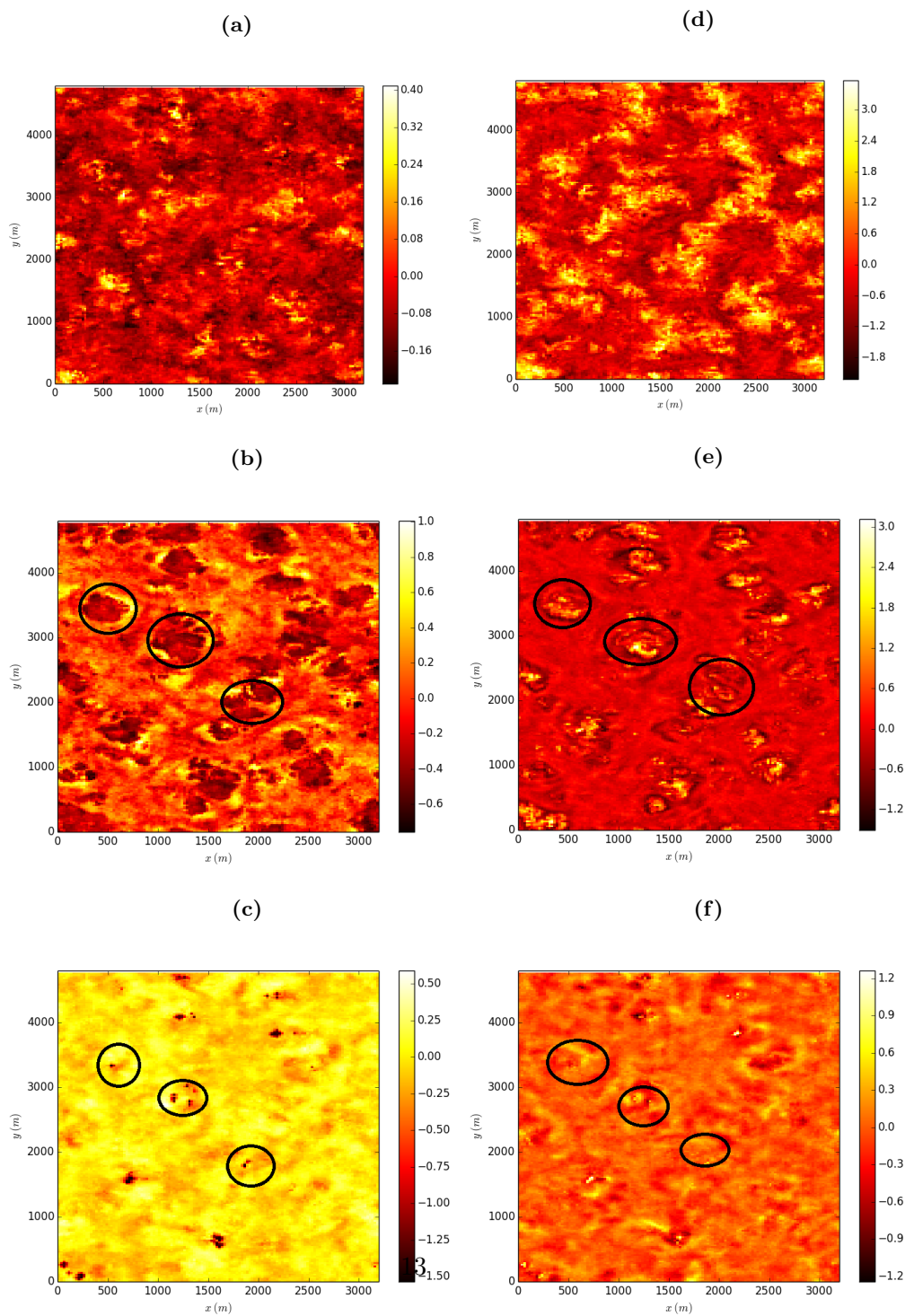
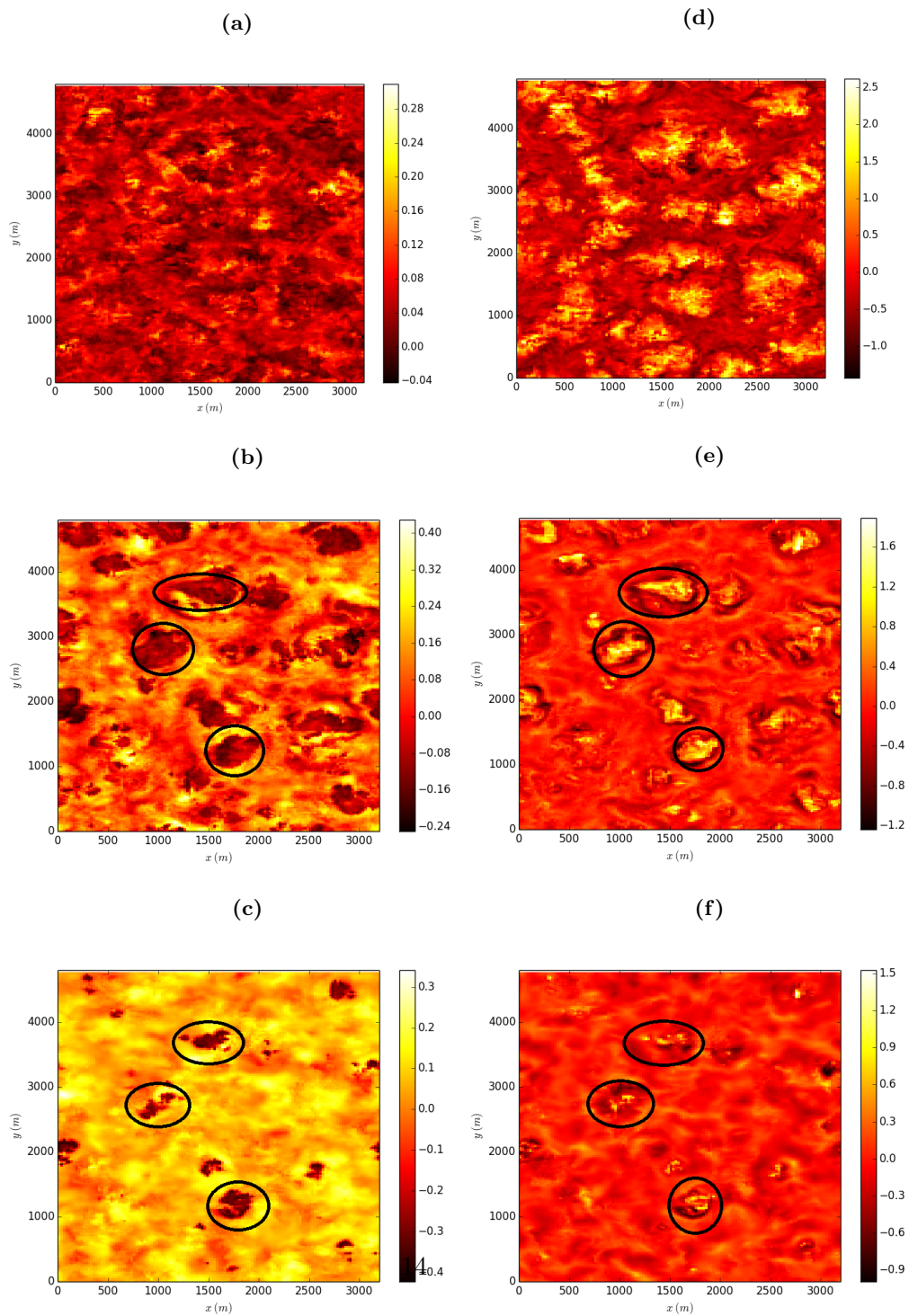


Figure 2.10: θ' (left) and w' (right) at 2 hours at h_0 (a,d), h (b,e) and h_1 (c,f)



2.4 Local Mixed Layer Heights (h_0^l)

Local θ profiles (Figures 2.11 and 2.12) exhibit a distinct ML before resuming γ but not always a clearly defined EL. There are sharp changes in the profile well into the free atmosphere, due possibly to waves, which render the gradient method for determining h^l unusable. Instead a linear regression method is used, whereby three lines representing: the ML, the EL and the upper lapse rate (γ), are fit to the profile according to the minimum residual sum of squares (RSS). Determining local ML height (h_0^l) was more straight forward than the local height of maximum potential temperature gradient (h^l) for the reasons stated above.

Figure 2.11 shows two local θ profiles where h_0^l is relatively high. A sharp interface is evident indicating that this is within an active plume impinging on the stable layer. In Figure 2.12 where h_0^l is relatively low a less defined interface indicates a point now outside a rising plume. Contour plots (Figure 2.13) show regions of high h_0^l corresponding to regions of upward moving relatively cool air at h .

The distribution of h_0^l is related to the depth of the entrainment layer (EL). Spread increases with increasing $\overline{w'\theta'_s}$ and decreases with increasing γ (Figure 2.14). When scaled by h (Figure 2.15), the local ML height distribution has spread that narrows with increased γ and seems relatively uninfluenced by change in $\overline{w'\theta'_s}$. The upper limit seems to be constant at about $1.1(\times h)$, whereas the lower limit varies depending on γ . Runs with lower h and narrower Δh have relatively larger spacing between bins and so higher numbers in each bin. The above supports the results outlined in Section 3.6.3.

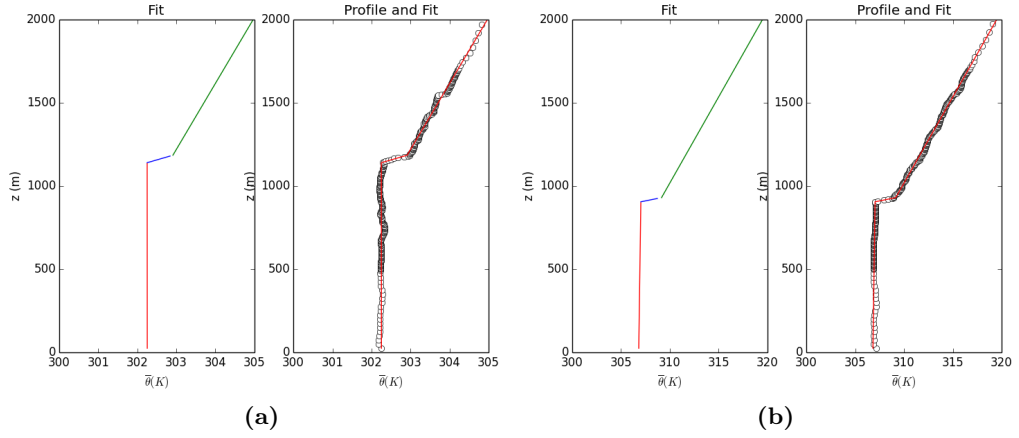


Figure 2.11: Local vertical θ profiles with 3-line fit for the 60/2.5 (a) and 150/10 (b) runs at points where h_0^l is high.

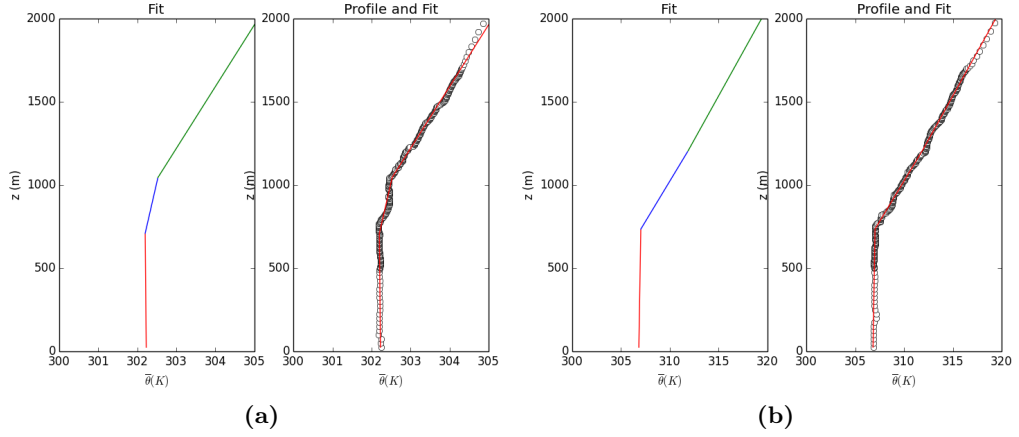


Figure 2.12: Local vertical θ profiles with 3-line fit for the 60/2.5 (a) and 150/10 (b) runs at points where h_0^l is low.

Figure 2.13: θ' (a,d), w' (b,e) at h_1 (c,f) and local ML height h_0^l at 2 hours for 60/2.5 (left) and 150/10 (right) runs

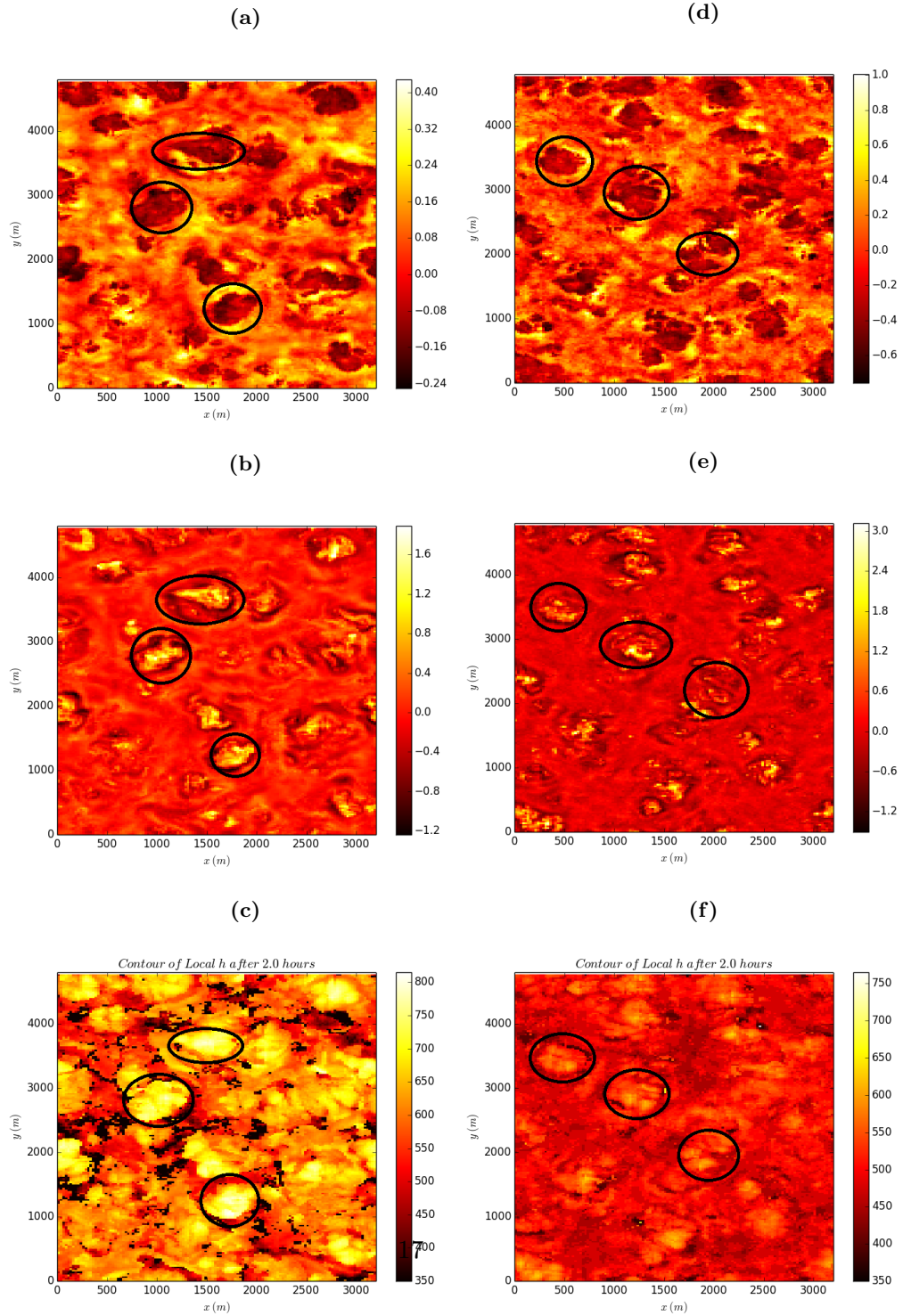


Figure 2.14: Histograms of h_0^l for $\overline{w'\theta'_s} = 150$ to $60(W/m^2)$ (a to c) and $\gamma = 10$ to $2.5(K/Km)$ (c to g) at 5 hours

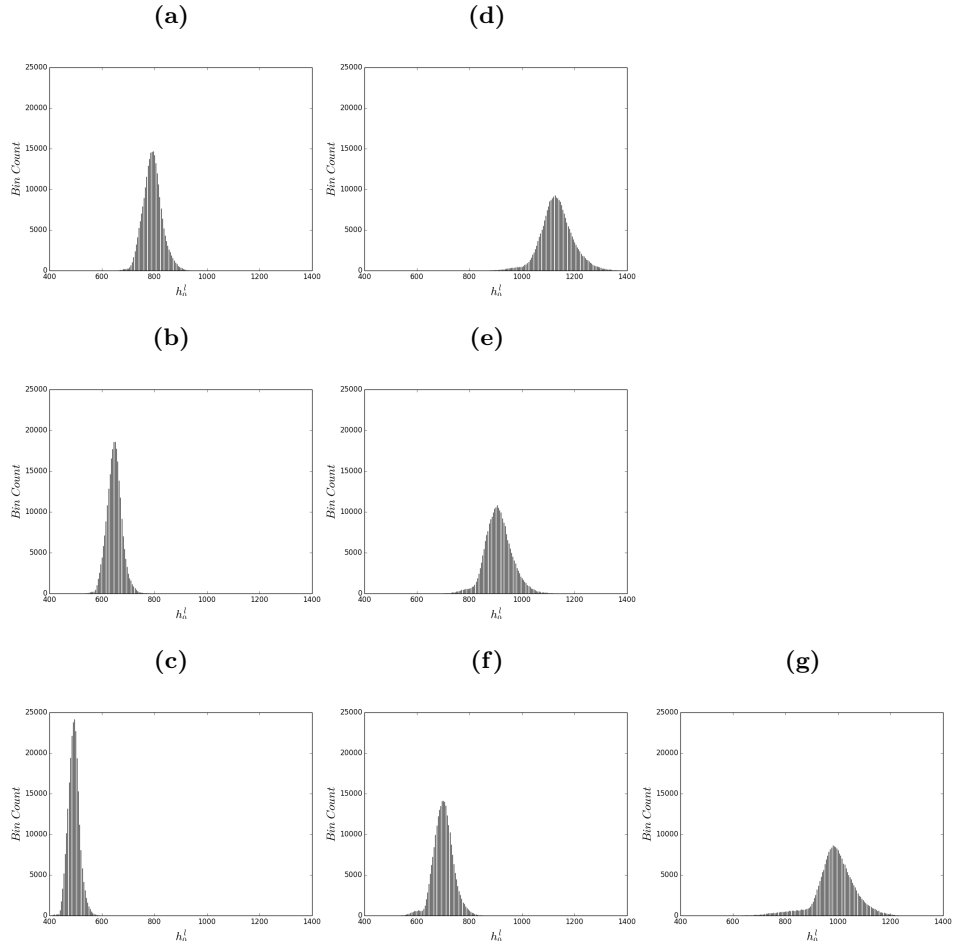
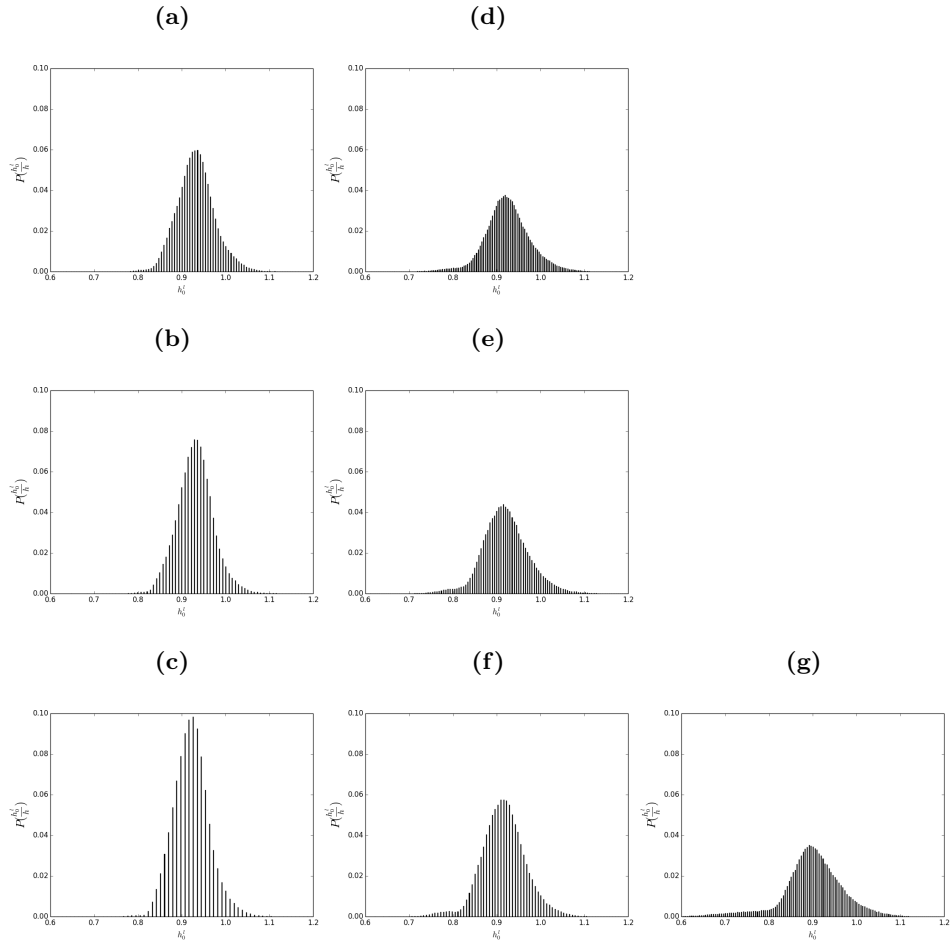


Figure 2.15: PDFs of $\frac{h_0^l}{h}$ for $\overline{w'\theta'_s} = 150$ to $60(W/m^2)$ (a to c) and $\gamma = 10$ to $2.5(K/Km)$ (c to g) at 5 hours



2.5 Flux Quadrants

As Sullivan et al. point out in [14] when broken out into four quadrants (Figure 2.16) the $\overline{w'\theta'}$ profiles have upper extrema above that of the total average profile (z_f). 2D histograms of the four quadrants are plotted at h_0 , h and h_1 to see how the distributions are influenced by changes in $\overline{w'\theta'}$ and γ .

At h_0 (Figure ??) fast updraughts are relatively warm. The spread in w' increases with increasing $\overline{w'\theta'}_s$ and decreases with increased γ . At h (Figure 2.16) the faster updraughts are now relatively cool and movement (both up and down) of warmer air from aloft becomes more prominent. The spread of w' and θ' both increase with increasing $\overline{w'\theta'}$ whereas that of θ' increases only slightly with increased stability. As expected stability inhibits both upward and downward w' .

Although the quadrant of overall largest magnitude is that of upward moving cool air, Sullivan et al.'s assertion in [14] that in the EL the heat flux is effectively due to downward moving warm air because the other three quadrants cancel, is found to be approximately true. At the top of the EL (Figure 2.19) velocities are damped and the distributions approach symmetry apart from some slow, cool, impinging up- and down-draughts as in Figure 2.13.

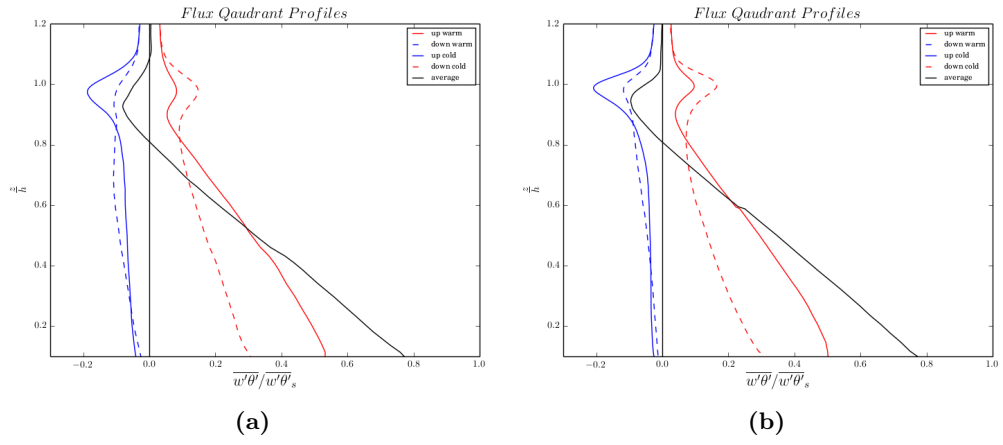


Figure 2.16: Scaled $\overline{w'\theta'}$ quadrant profiles at 5 hours for the 60/2.5 (a) and 150/10 (b) run

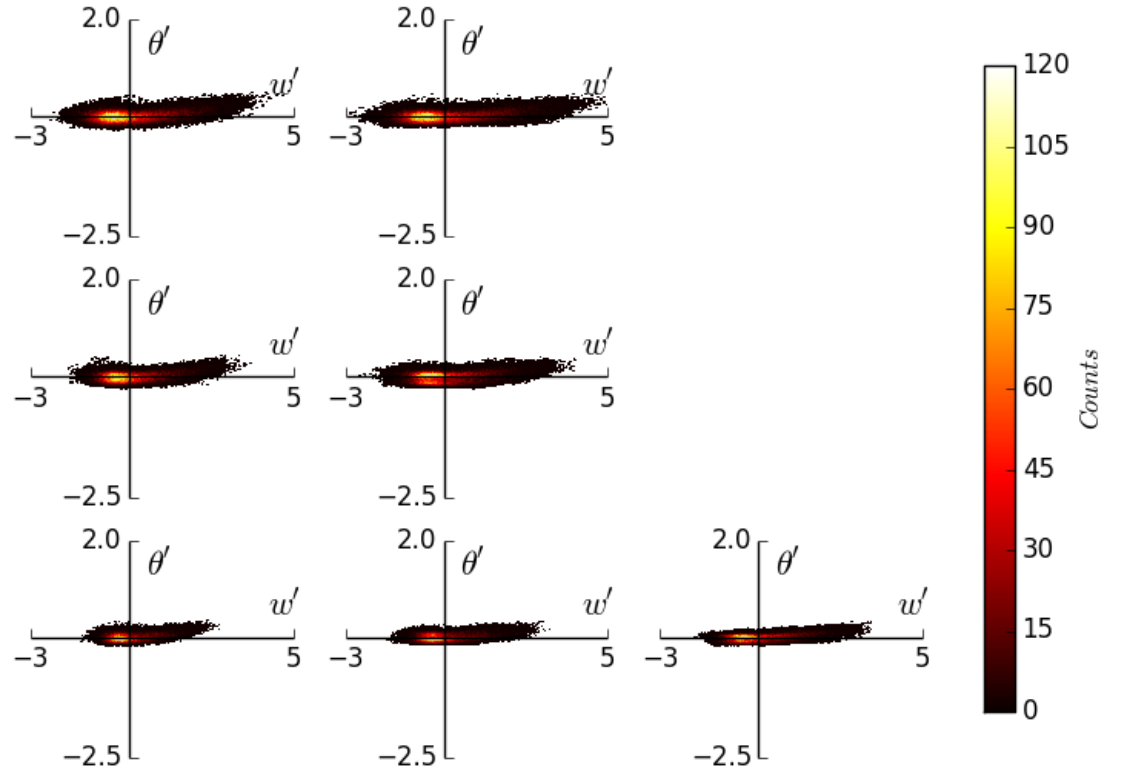


Figure 2.17: $\overline{w'\theta'}$ quadrants at h_0 for $w'\theta' = 150 - 60(W/m^2)$ (top-bottom) and $\gamma = 10 - 2.5(K/Km)$ (left-right) at 5 hours

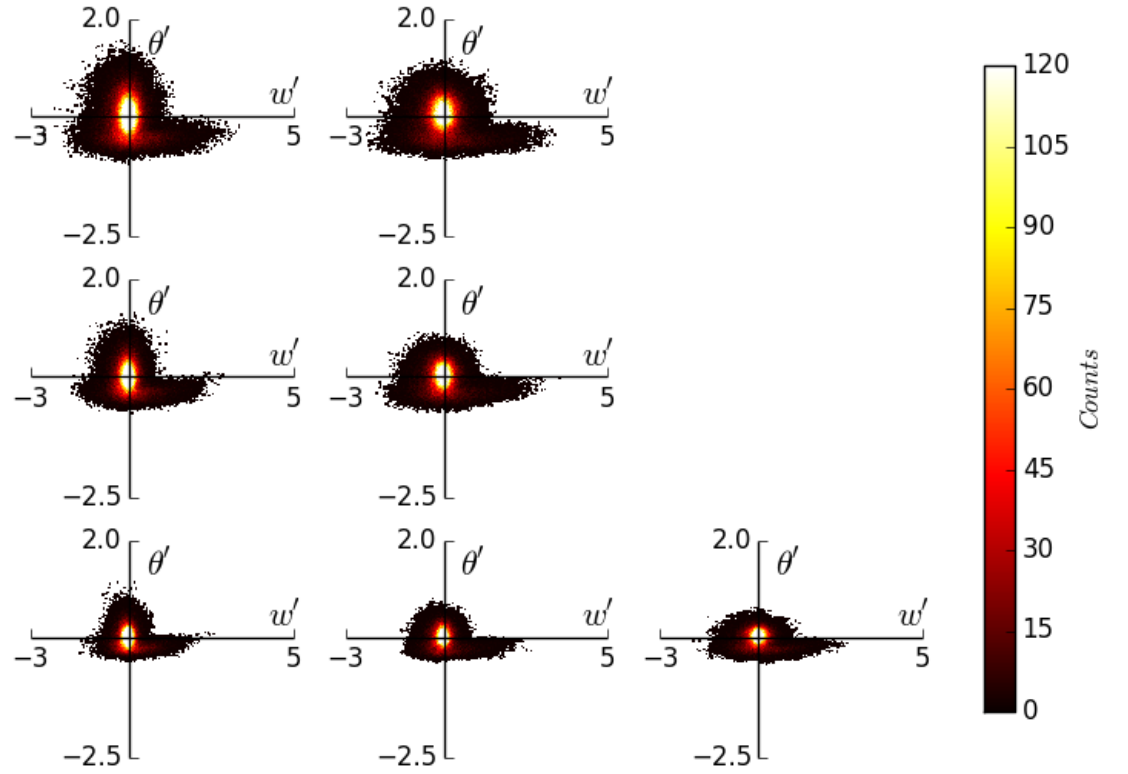
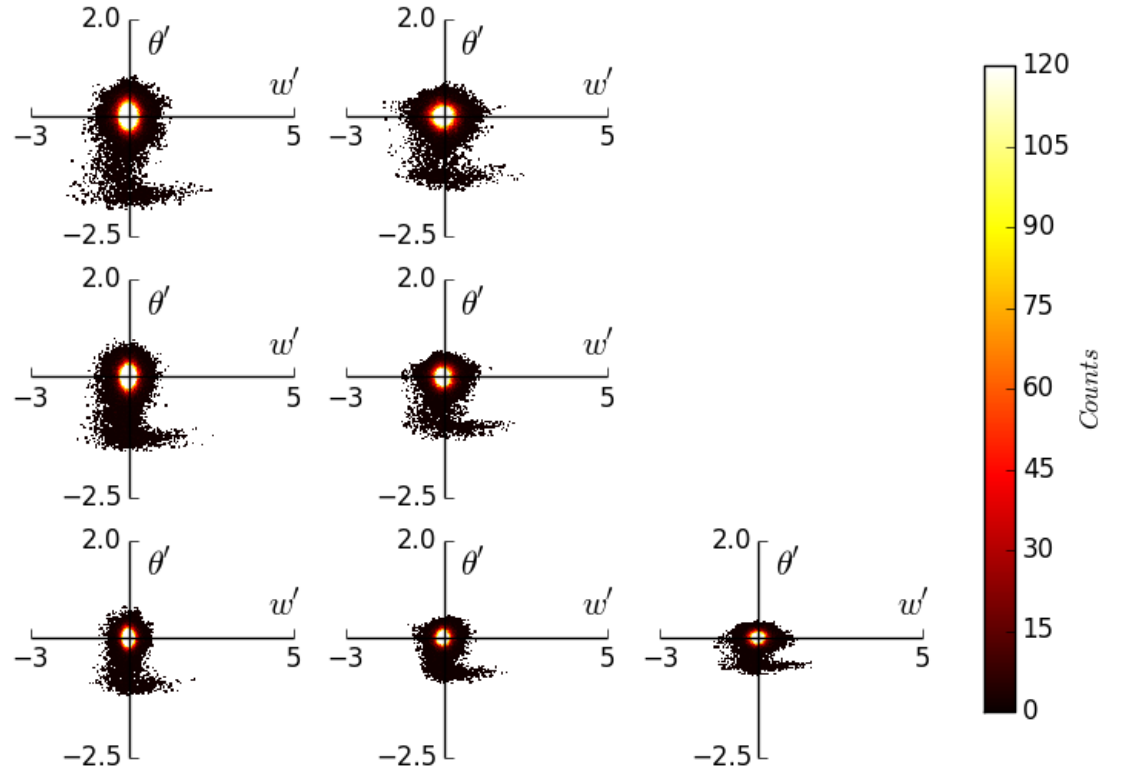


Figure 2.18: $\overline{w'\theta'}$ quadrants at h for $w'\theta' = 150 - 60 \text{ (W/m}^2\text{)}$ (top - bottom) and $\gamma = 10 - 2.5 \text{ (K/Km)}$ (left - right) at 5 hours

Figure 2.19: $\overline{w'\theta'}$ quadrants at h_1 for $w'\theta' = 150$ to $60(\text{W}/\text{m}^2)$ (top to bottom) and $\gamma = 10$ to $2.5(\text{K}/\text{Km})$ (left to right) at 5 hours



2.6 h and Δh based on Average Profiles

2.6.1 Reminder of Relevant Definitions

Here we define CBL height h as the point at which $\frac{\partial \bar{\theta}}{\partial z}$ is maximum and the EL limits: h_0 the point at which $\frac{\partial \bar{\theta}}{\partial z}$ first exceeds a threshold and h_1 the point at which $\frac{\partial \bar{\theta}}{\partial z}$ resumes γ . The temperature jump $\Delta\theta$ is the difference across the EL.

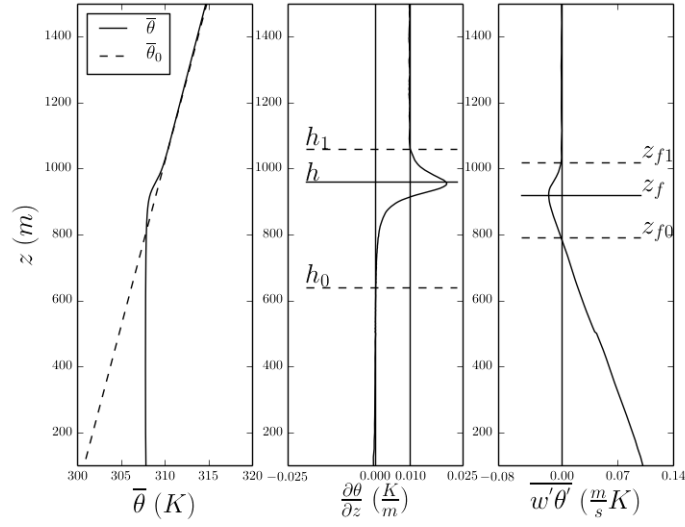


Figure 2.20: Height Definitions

Description	This Study	Sullivan et al. [14]	Fedorovich et al. [4]
CBL Height	h	h	z_f
Temperature Jump	$\Delta\theta = \bar{\theta}(h_1) - \bar{\theta}(h_0)$	$\Delta\theta = \bar{\theta}(z_{f1}) - \bar{\theta}(z_f)$	$\Delta b = b_0(z_f) - b(z_f)$
			$\delta b = b(z_{f1}) - b(z_{f0})$
Convective Velocity Scale	$w_* = \frac{(hB_s)^{\frac{1}{3}}}{B_s} = \frac{g}{\theta_{ML}} w' \theta'_s$	$w_* = \frac{(hB_s)^{\frac{1}{3}}}{B_s} = \frac{g}{\theta_{ML}} w' \theta'_s$	$w_* = (z_f B_s)^{\frac{1}{3}}$
Richardson Number	$Ri = \frac{\Delta\theta h}{w_*^2}$	$Ri = \frac{\Delta\theta h}{w_*^2}$	$Ri_{\Delta b} = \frac{\Delta b z_f}{w_*^2},$ $Ri_{\delta b} = \frac{\delta b_i z_f}{w_*^2}$

Table 2.3: Comparison of relevant definitions with those from key publications

2.6.2 $\frac{w_e}{w^*}$ vs Ri^{-1}

Covective Boundary Layer (CBL) height (h) (Figure 2.21) grows rapidly initially with a steadily decreasing rate and relates to the square root of time (Figure 2.22). It is found to be proportionate to the height of minimum flux (z_f) (Figure 2.23).

Inverse Richardson Number (Ri^{-1}) decreases with respect to time and clusters according to γ . (Figure 2.24). The entrainment rate ($w_e = \frac{dh}{dt}$) is determined from the slope of a second order polynomial fit to $h(time)$ (Figure 2.21). When scaled by (w^*) it is a roughly linear function of Ri^{-1} (Figure 2.25).

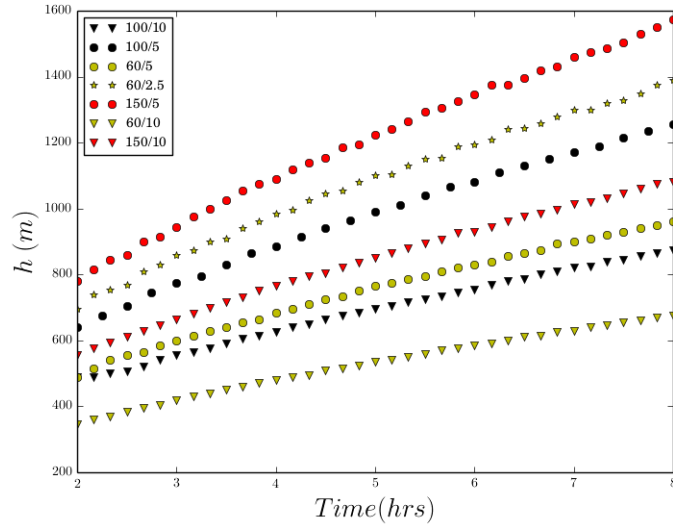


Figure 2.21: h vs time for all runs

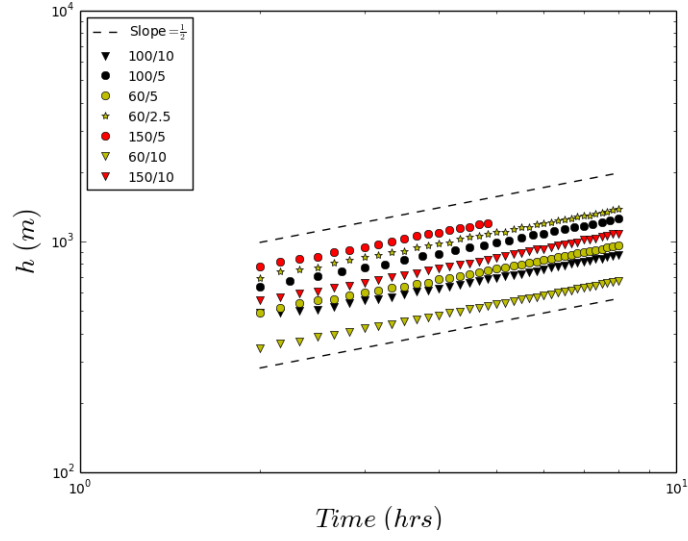


Figure 2.22: Log-Log plot of h vs time for all runs

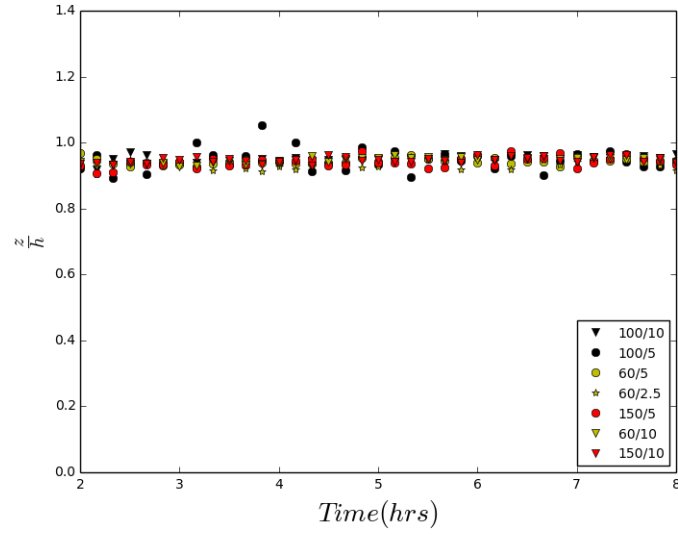


Figure 2.23: $\frac{z_f}{h}$ vs Time

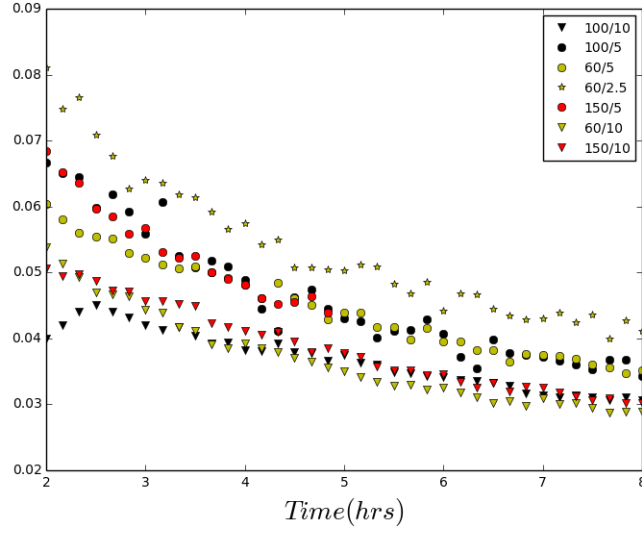


Figure 2.24: Inverse bulk Richardson Number vs time

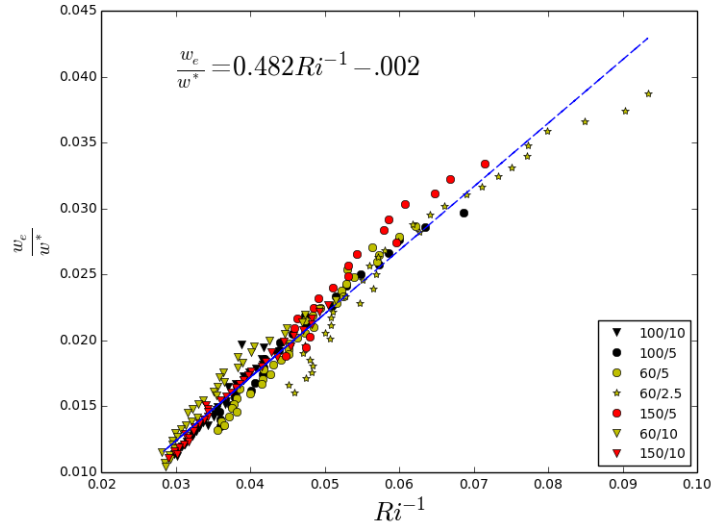


Figure 2.25: Scaled Entrainment rate vs inverse Richardson Number (Ri)

2.6.3 $\frac{\Delta h}{h}$ vs Ri^{-1}

The scaled upper EL limits ($\frac{h_1}{h}$) collapse well in Figure 2.26 to an initial value of approximately 1.15, decreasing to about 1.1. $\frac{h_0}{h}$ s appear grouped according to γ and increase with respect to time. So overall the scaled EL appears to narrow with time. The scaled flux based EL (z_{f0} and z_{f1}) appears to remain constant with respect to time in Figure 2.27.

The lower entrainment layer limit h_0 is the point at which the vertical $\frac{\partial \bar{\theta}}{\partial z}$ exceeds a threshold (.0002) chosen such that it is positive, and at least an order of magnitude smaller than γ . Although the resulting scaled EL depth decreases with increasing Ri grouping according to γ is evident in Figure 2.29.

To explore how varying the threshold value affects the relationship between scaled EL depth and Richardson number (Ri), plots analogous to Figure 2.29 were produced at two additional thresholds. A higher threshold value (.0004) results in a higher h_0 (Figure 2.30) and so a narrower EL but a similar grouping according to γ (Figure 2.31). A lower threshold value (.0001) results in a lower h_0 (Figure 2.32) but also similar grouping according to γ (Figure 2.33).

When the height definitions are based on the scaled vertical $\frac{\partial \bar{\theta}}{\partial z}$ i.e. $\frac{\partial \bar{\theta}}{\partial z}/\gamma$ profile, only h_0 changes and for clarity we call this EL depth Δh^* and the revised Richardson number Ri^* . The curves now collapse and scaled EL depth is seen to decrease with increasing Ri^* (Figures 2.34 to 2.36).

There is a slight collapsing effect on the scaled entrainment rate vs Ri relationship when the heights are defined based on the scaled vertical potential temperature gradient $\frac{\partial \bar{\theta}}{\partial z}/\gamma$ profile in Figure 2.37.

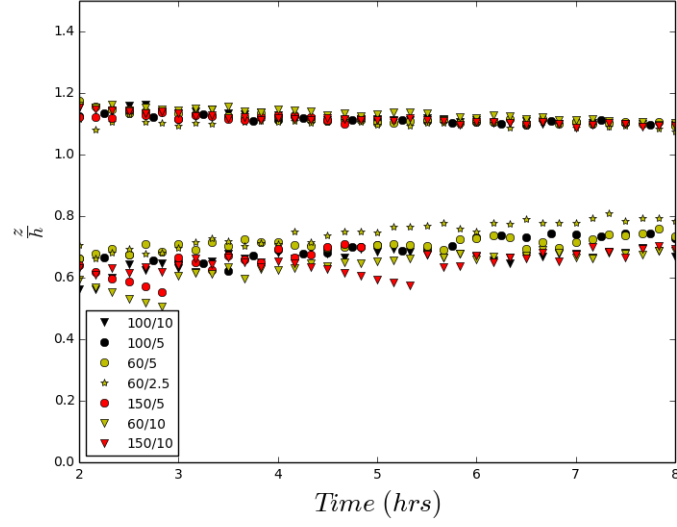


Figure 2.26: Scaled Entrainment Layer limits ($\frac{h_1}{h}$ and $\frac{h_0}{h}$) vs time

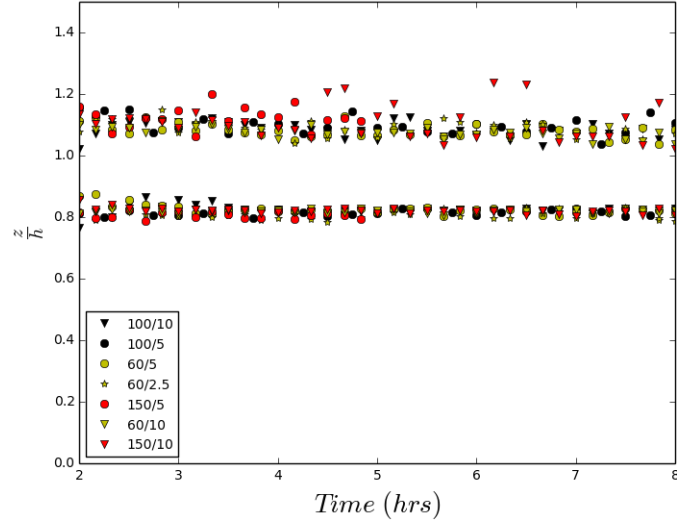


Figure 2.27: Scaled Entrainment Layer limits (z_{f1} and z_{f0}) vs time

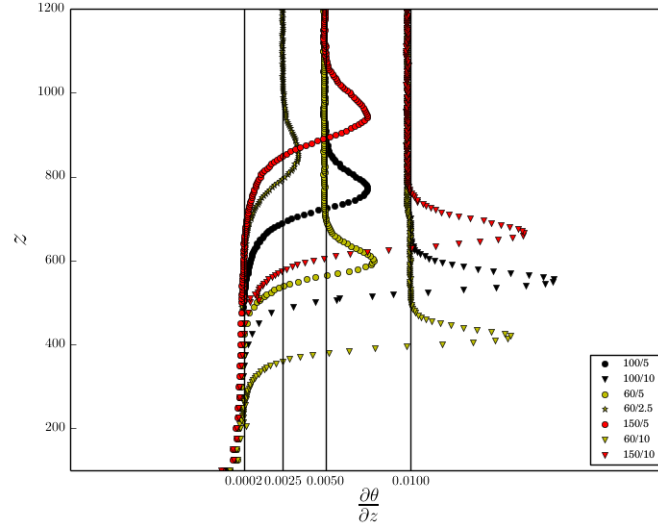


Figure 2.28: Vertical $\frac{\partial \bar{\theta}}{\partial z}$ profiles with threshold at .0002

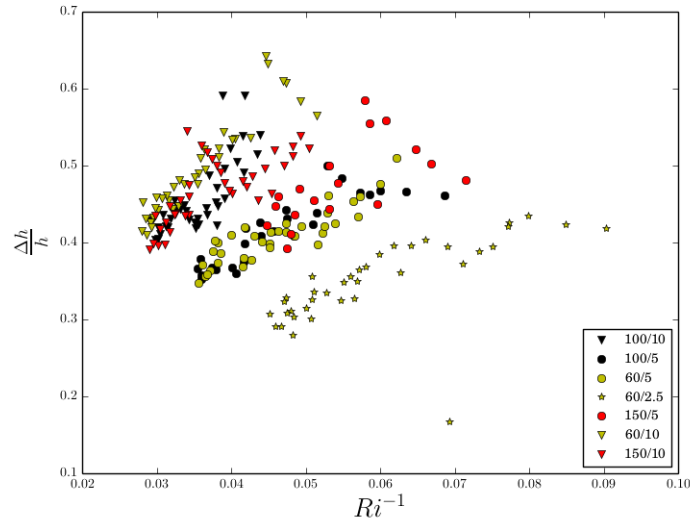


Figure 2.29: Scaled EL depth vs inverse bulk Richardson Number with threshold at .0002

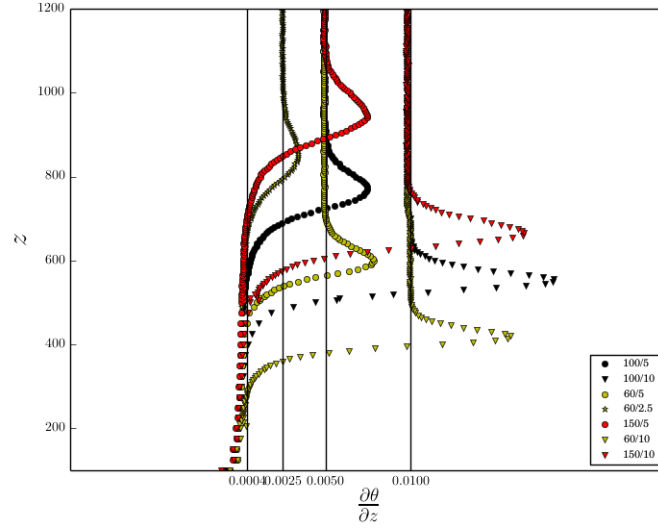


Figure 2.30: Vertical $\frac{\partial \bar{\theta}}{\partial z}$ profiles with threshold at .0004

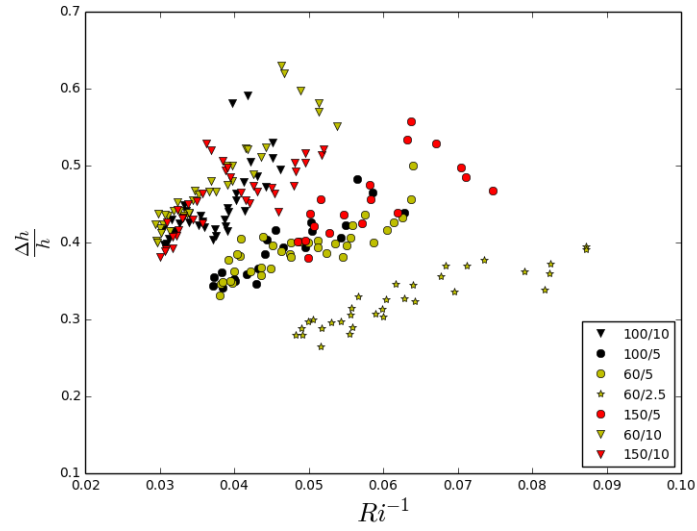


Figure 2.31: Scaled EL depth vs inverse Richardson Number with threshold at .0004

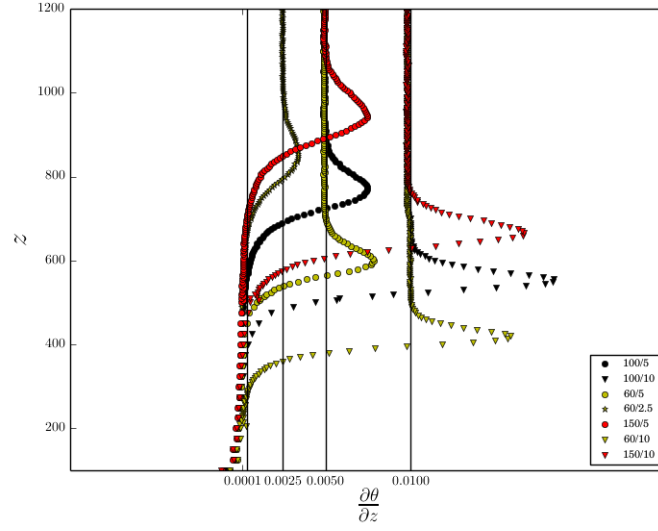


Figure 2.32: Vertical $\frac{\partial \bar{\theta}}{\partial z}$ profiles with threshold at .0001

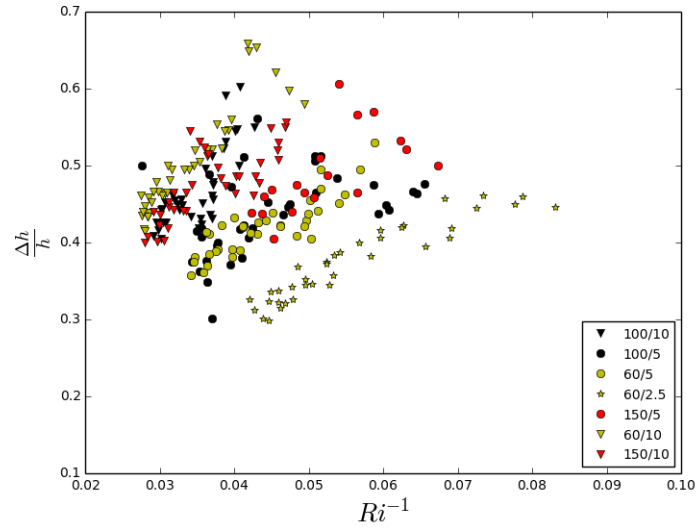


Figure 2.33: Scaled EL depth vs inverse bulk Richardson Number with threshold at .0001

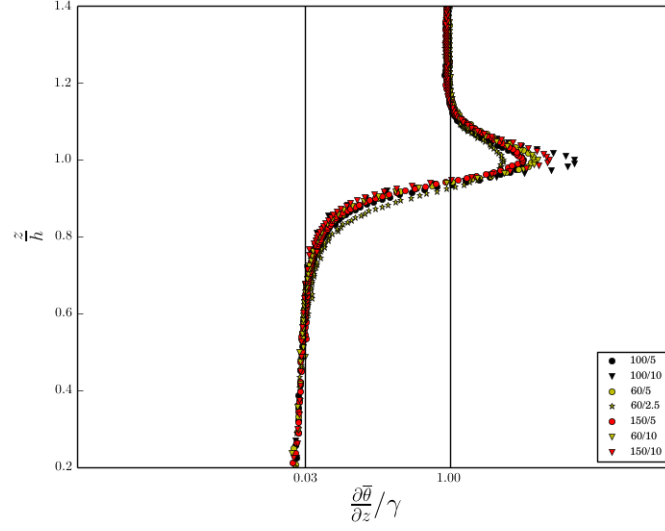


Figure 2.34: Scaled vertical $\frac{\partial \bar{\theta}}{\partial z}$ profiles with threshold at .03

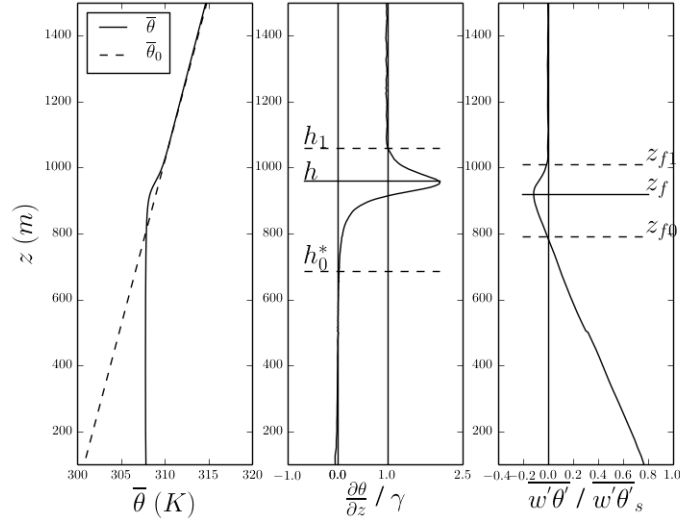


Figure 2.35: Revised height definitions based on scaled $\frac{\partial \bar{\theta}}{\partial z}$ profiles with threshold at .03

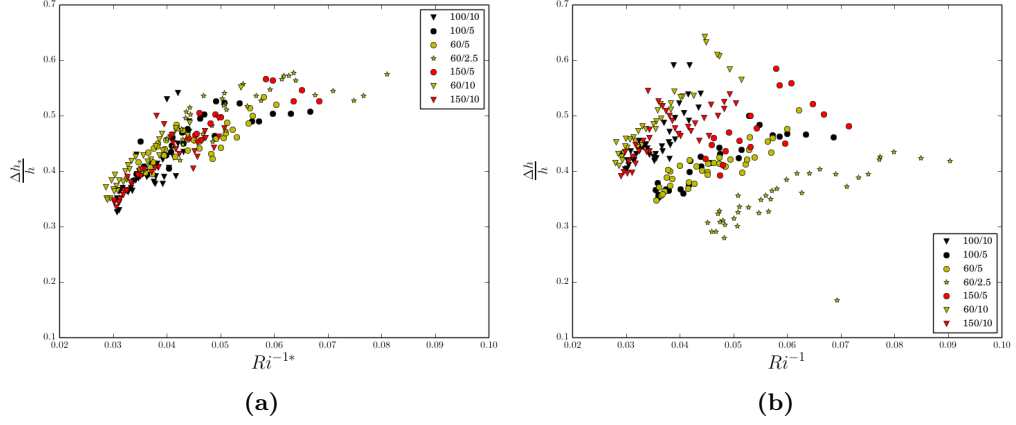


Figure 2.36: Scaled EL Depths vs inverse bulk Richardson number based on scaled $\frac{\partial \theta}{\partial z}$ (a) and $\frac{\partial \theta}{\partial z}$ (b)

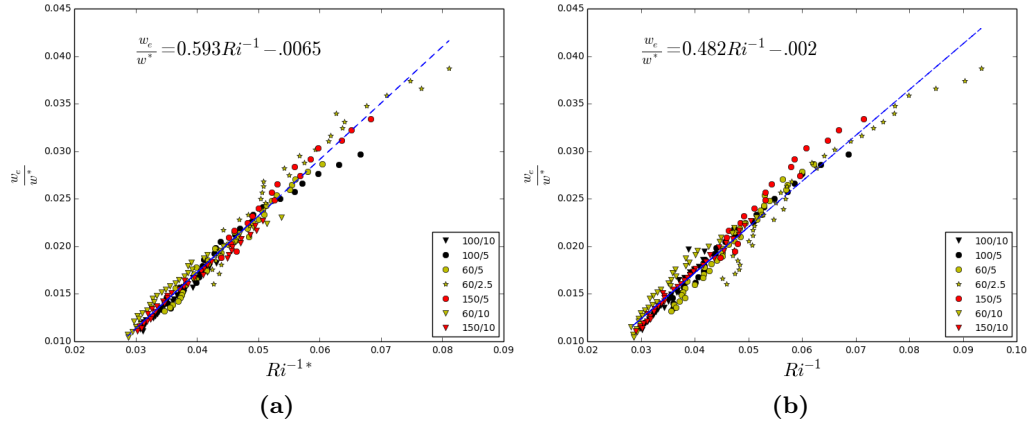


Figure 2.37: Scaled Entrainment Rate vs inverse bulk Richardson number based on scaled $\frac{\partial \theta}{\partial z}$ (a) and $\frac{\partial \theta}{\partial z}$ (b)

Chapter 3

discussion

3.1 Description of Runs

The domain for each individual case is small relative to that used by Sullivan et al. in [14], Federovich et al. in [4] and Brooks and Fowler in [2] i.e. $5Km \times 5Km$ in the horizontal. Sullivan et al. ([14]) did a higher resolution run on a $3Km \times 3Km$ horizontal domain and noticed a higher convective boundary layer height (h) but similar slope in h with respect to scaled time when compared with the analogous run on a larger domain with lower resolution. They speculated the smaller domain enforced a smaller limit on plume size, thus influencing h . But according to Sullivan and Patton ([13]) grid size also impacts h .

Sullivan et al.'s ([14]) grid spacing for most of their runs was $\Delta x, y = 33.3$, $\Delta z = 10$ except for the run on the smaller domain which had $\Delta x, y = 15$, $\Delta z = 6.67$. The highest resolution Federovich et al. used in [4] was $\Delta x, y = 50$ and $\Delta z = 20$. Brooks and Fowler in [2] used $\Delta x, y = 50$ and $\Delta z = 12$ except in resolution test runs where they used $\Delta x, y = 25$ and $\Delta z = 7.27$. So the vertical resolution around the entrainment region in this study ($\Delta z = 5m$) is higher than the other LES studies. Both Sullivan et al. ([14]) and Brooks and Fowler ([2]) use varying grids in the vertical, such that the region around the entrainment layer (EL) is of higher resolution than

elsewhere. We do the same in this study and noticed slight kinks in some of the profiles where the transition to and from higher resolution occurs. We will perform one run on a uniform vertical grid at $\Delta z = 5m$ to verify that this does not effect the results.

Sullivan et al.'s ([14]) initialized with a layer of constant potential temperature topped by an inversion topped by a constant lapse rate ($\gamma \approx 2.5K/Km$). They applied constant average surface heat fluxes ($\overline{w'\theta'}_s$) ranging from about 20–450 *Watts/m²*. Brooks and Fowler ([2]) followed suit, in that their range of Richardson numbers (Ri) resulted from variation of initial inversion ($\Delta\theta$) strength and average surface heat flux ($\overline{w'\theta'}_s$). Federovich et al. in [4] start with a finite layer of constant average potential temperature ($\bar{\theta}$) above which there was a constant lapse rate which they varied from 1 – 10 *K/Km*. In this study we begin with a constant $\overline{w'\theta'}_s$ acting against uniform potential temperature lapse rate. Schmidt and Schumann point out in [9] that as a convectively mixed layer (ML) grows against a stable lapse rate (γ) overshoot of the plumes to buoyancy levels above their own, and subsequent entrainment causes a sharp temperature gradient. (see Table 2.1)

3.2 Relevant Definitions

See Table 2.2.

Sullivan et al. ([14]) compared four methods of determining CBL height, two of which they based on the vertical average heat flux ($\overline{w'\theta'}$) profile. For both, the time-series were a lot less smooth than that for z_f determined in this study. Their gradient and contour methods produced smoother time-series plots. The former, they determined from the horizontal average of the local heights of maximum vertical potential temperature gradient. Description of the contour method will be omitted since it is not directly useful. Their gradient based height is consistently higher than the heat flux based definitions i.e. the flux based definition overall is about 0.9 times the gradient definition. This is in line with the findings of this study. They did

not focus on EL depth. For their Richardson number (Ri) they calculated $\Delta\theta = \bar{\theta}(z_{f1}) - \bar{\theta}(z_f)$. This value is likely to be smaller than, and not necessarily proportionally to the $\Delta\theta$ used in this study.

Federovich et al. in [4] determined CBL height and EL depth from the horizontal and time ($100 \times 2s$) averaged vertical $\overline{w'\theta'}$ profiles. They used two difference buoyancy ($\frac{g\bar{\theta}}{\bar{\theta}_{ML}}$) jumps: $\Delta b = \bar{\theta}_0 z_f - \bar{\theta} z_{f0}$ for comparison with the zero order model and $\delta\theta = \bar{\theta} z_{f1} - \bar{\theta} z_{f0}$ for comparison with the first order model and analysis of the EL.

Brooks and Fowler ([2]) used tracer concentration profiles and compare a number of different corresponding CBL height definitions. Although their height and temperature jump used to calculate the Richardson number (Ri) are quite different, their scaling relations based on the fluxed based definitions can be compared to those in this study. For example the corresponding scaled entrainment rate vs Ri plot has a lot of scatter.

The definitions that perform best in relation to Ri for Brooks and Fowler ([2]) are those based on the means of locally determined heights. That based on the domain averaged tracer profile, ie the point of maximum vertical gradient, is directly comparable to our h . Although, this last definition does not produce a plot as correlated as ours.

Their scaled statistical EL definitions based on the local vertical gradient and the local wavelet covariance decrease with increasing Ri similarly to ours, but their flux based definition ($2 \times (z_{f1} - z_f)$) show slight and opposite trends when averaged differently. The latter is in line with what we found.

The height definitions in this study are all based on the average vertical potential temperature gradient ($\bar{\theta}$). It seems to be assumed that the region, where the average potential temperature increases significantly from its mixed layer (ML) value through the maximum to that of the free atmosphere, corresponds to the EL as enclosed by the zero levels in the average

potential temperature flux profiles (Deardorff [3], Federovich et al. [4], Garcia and Mellado [5]). But the average potential temperature profile is not used to quantitatively define the EL.

Brooks and Fowler ([2]) discuss the draw-backs of defining the EL based on the gradient of an average tracer profile. Specifically the inconsistency in the size of the gradient relative to a maximum, at the average EL limits as defined based on the local limits. They found the relative size had significant scatter and varied according to Ri. Their maximum and the manner in which they determine is not reproducible in our framework but their conclusion could serve as a caution.

Since in the ML on average there is a gradual increase through zero in average potential temperature above the surface layer, rather than a region where the gradient is zero. So a threshold value must be chosen to identify the lower limit of the EL. This threshold should be less than the upper lapse rate (γ), positive and consistent for all runs. It was chosen by looking at the gradient profile and selecting a point which looked reasonable. The principal result was plotted at three different thresholds based on the unscaled gradient ($\frac{\partial \bar{\theta}}{\partial z}$) profiles.

The upper EL limit is defined as the point at which the average vertical potential temperature gradient resumes γ . These two limits then represent: the point above the surface layer at which the air on average begins to be less turbulently mixed, and the lowest point at which the air is unaffected as yet by the convected turbulence. Our principal length scale h is the point at which the gradient is maximum i.e. the point at which on average the air differs greatest from that directly above it. Our $\Delta\theta$ is the difference in average potential temperature ($\bar{\theta}$) over the EL. We compare h with the fluxed based definitions.

3.3 Verifying the Model Output

3.3.1 Time till well-mixed

To establish statistically steady turbulent flow Sullivan et al. in [14] ran from the same random initial conditions on their coarse grid for more than ten eddy turnover times. Then they switched on the nested high resolution grid and continued for another 4 Odie turnovers. Brooks and Fowler ([2]) waited 2 simulated hours before they judged the turbulence to be fully developed. To initialize turbulence they added a small random perturbation to the temperature field.

Federovich et al. ([4]) focus on the attainment of a quasi-steady state regime within which their zero order entrainment equation holds. Their derivation also hinges upon parametrizations for turbulent kinetic energy (e) and dissipation (ϵ):

$$e = w^{*2} \Psi_e \left(\frac{z}{z_i} \right) \quad \epsilon = \frac{w^{*3}}{z_i} \Psi_\epsilon \left(\frac{z}{z_i} \right) \quad (3.1)$$

Where the two functions of dimensionless height integrate over the CBL to constants, for example

$$\int_0^{z_i} \frac{e}{w^{*2}} dz = C_e \quad (3.2)$$

In the referenced regime, CBL growth is much slower than the convective velocity scale (w^*), there is a constant entrainment ratio $-\frac{\overline{w'\theta'_{min}}}{\overline{w'\theta'_s}}$ and change in the total e and it's escape from the boundary layer through waves are negligible relative to the buoyant production and dissipation rate. The resulting entrainment equation predicts a $\frac{1}{2}$ power law relationship between the normalized height, $z_i B_s^{-\frac{1}{2}} N^{\frac{3}{2}}$ and time tN . Since variation in $\bar{\theta}$ results in less than 3 percent variation in N , when the surface heat flux B_s and γ are constant this roughly translates to a $\frac{1}{2}$ power law relationship between h and time. In our study we find this to be the case (see Figure 2.23).

We also observe self similarity of the scaled flux profiles, and so a constant entrainment ratio (see Figure 2.4). By 2 hours of simulated time, at least 10 eddy turnover times have elapsed and by 3 hours the EL is fully within the region of high vertical resolution. Worth noting is the collapse in scaled time curves from 7 to 3 according to upper lapse rate (γ) (see Figure 2.2).

3.3.2 FFT Energy Spectra

Based on the scalar FFT energy plots taken at the top of the ML there is a cascade from the larger to the smaller scales following the $-\frac{5}{3}$ power law (see Figure 2.6). The CBL is fully turbulent at this point but further into the entrainment layer (EL) there are large areas of little or no vertical velocity interspersed with isolated impinging plumes. So the dominant structures are smaller and there is a steeper decay to the lower scales. In this the FFT plots and the contour plots in Figures 2.10 and 2.9 compliment each other. Furthermore there seems to be adequate scale separation between the dominant turbulent structures and the grid size, as well as isotropic turbulence.

3.3.3 Ensemble and horizontally averaged vertical Potential Temperature $\bar{\theta}$ and Heat Flux profiles $\overline{w'\theta'}$

Schmidt and Schumann point out in [9] that as a convectively mixed layer (ML) grows against a stable lapse rate (γ) overshoot of the plumes to levels above their buoyancy causes a sharp temperature gradient. The sharpest vertical gradient in the area averaged potential temperature ($\bar{\theta}$) profile corresponds to the vertical level at which the average potential temperature (Figure 2.7) differs greatest from that one level above. Once a plume has overshoot, envelopment or pinching off (Sullivan et al. [14]) of warm air from above causes a more gradual increase in temperature. Where this occurs is regarded here as the entrainment layer EL. In the averaged potential temperature profile it is represented by an increase in the vertical gradient. On the horizontal plane it would be composed of areas of ML air interspersed with pockets of warmer air from above. The ratio of ML to stable air in-

creases with proximity to the ML. This progression is seen in the average profile as a decrease in the vertical gradient to close to zero (Figure 2.1). Our average potential temperature profiles in Figure 2.7 show a well mixed ML overshooting and growing against γ . CBL growth increases with $\overline{w'\theta'_s}$ and is inhibited by γ . The ML warming rate is strongly influenced by $\overline{w'\theta'_s}$ and γ .

The vertical $\overline{w'\theta'}$ profiles in Figure 2.8 assume the expected shape becoming negative in the EL where the upward moving thermals are relatively cooler than the horizontal average and there is also downward moving warmer air that has been pinched off or folded in. Like Sullivan et al. in [14] and Federovich et al. in [4] we notice the entrainment ratio is less than .2 ($\approx .1$) for all runs but seems to increase with increased γ inline with Sorbjan's assertion in [10] that moments of θ' depend on γ . Otherwise, there seems to be self similarity in time and across runs when scaled by $\overline{w'\theta'_s}$ and plotted against scaled height. So the scaled depth of the region of negative $\overline{w'\theta'}$ seems more or less constant whereas Federovich et al. in [4] seem to show a decrease from about .6 to about .2 with increasing Ri and Brooks and Fowler with their slightly different definition in [2] seem to observe slight and contrasting trends with respect to Ri depending on whether the output is time averaged or not.

3.3.4 Visualization of Structures within the Entrainment Layer

Sullivan et al. in [14] show both horizontal and vertical cross sections of their domain within the EL around the inversion (h). Horizontal cross sections of vertical velocity and temperature perturbations clearly show coherent structures with both relatively warm and cool air, associated with up-and-downward velocity. Vertical cross sections show impinging plumes and pockets of trapped warmer air. The weak inversion case seems to show convective overturning with apparent folding of warm stable air. The strong inversion case shows less deformation of the inversion interface and the entrainment event shown in the vertical cross section seems to occur via a narrow downward wisp associated with an impinging plume. In both cases,

the downward motion of air from above is closely associated with upward moving impinging plumes.

In our contours of w' and θ' we see the almost spoke like pattern characteristic of the mixed layer (Schmidt and Schumann [9]) at the lower limit of the EL and then distinct plumes become clearer at the inversion and above, where there are coherent areas of warmer and cooler air associated up and downward vertical velocity perturbations (Figures 2.9 and 2.10). This progression is similar to that seen in [5] by Garcia and Mellado. We do see bigger clearer regions of upward moving air in the weak stability case as compared to the the strong stability case. There are pockets of warmer air close to and around the impinging cooler plumes, in line with the concept of wisps being pinched off, or enfolded.

3.4 Local Mixed Layer Heights (h_0^l)

Sullivan et al. [14] used a centred differencing gradient method for determining local CBL height and observed the distributions of $z'_i = z_i - \langle z_i \rangle$. They observed positive skew in their weak stability cases which they speculated was due to a small number of high reaching plumes. We initially tried a similar method and noticed positive skew, which we found corresponded to local points where the upper variability exceeded the gradient between the ML and the upper atmosphere. So for our purposes the gradient method was rendered unusable

The point of maximum vertical gradient in a tracer profile should correspond to that in a potential temperature profile but the profiles can be quite different. For example a Lidar back-scatter profile which corresponds directly to tracer concentration profile, has a high value in the ML and a low value in the upper atmosphere, similar to step function. Usually the variability within these regions is a lot smaller than that over the transition region between the two. So the transition region can be identified using a wavelet of dilation corresponding the the depth of the transition zone. This is clearly

shown by Brooks in [1] who uses such a wavelet to identify the local EL and then one with narrower dilation to identify the EL limits. The gradient method can also be applied to a Lidar profile but again this can be noisy. Steyn et al. in [12] overcame this by fitting smooth idealized curve to the profile.

In line with this last method, we fit a three lines to the local profile representing the ML, EL and upper layer of constant γ based on the multilinear regression method outlined by Vieth in [16]. This works well with our very simple set up, IE, each local profile consists of a distinct ML and upper region of constant γ . Locally there is not always a clear EL. At points where there is neither a sharp gradient nor a clear EL and some variation in the slope within the ML, a test was needed on the slope of the second line to see if it was significantly less γ . If so, it was considered to be part of the ML.

Brooks and Fowler’s three statistically based entrainment zone limits in [2] showed decreasing trend with increase in Ri. Their resulting scaled EL is a lot narrower than that based on our $\frac{\partial \bar{\theta}}{\partial z}$ profile i.e. .05 - 1.5, and even seems narrower than what would be the 5th and 95th percentile of our local ML heights (see Figure 2.15). Their lowest inversion strength seems to be 1 degree over 100 meters (IE .01 per meter) which is the same as our maximum stability, except of course ours is constant, and their highest is 10 times that. But their lapse rate above is a lot lower ($3k/Km$). So, this difference cannot simply be explained in terms of inversion strength.

We see that the local profiles are very different to the average profile and that local profiles differ from each other (Figures 2.11 and 2.12). The EL is an inherently average phenomena i.e. the range in space or, the range in time, over which the plume heights vary. So it is possible to see a local EL. For example in Figure 2.12 (a) we see a region above the ML which is clearly not part of the stable air above. Here, we can speculate that a plume previously had reached that point and some entrainment of warmer air from above had occurred.

Overall Sullivan et al. [14] show decreased variation in the local heights, with increased Ri as we do. Based on the histograms of our local ML heights in Figure 2.14 we see the range or spread increases with increased $\overline{w'\theta'}_s$ and decreases with increased γ . When scaled by h in Figure 2.15 the spread seems only influenced by γ . So once again there is a cancellation of the effects of $\overline{w'\theta'}_s$ once h is introduced.

3.5 Flux Quadrants

The shape of the average potential temperature profile evolves according to the temperature flux profile. In particular warming in the entrainment layer (EL), and upper mixed layer (ML) is related to the flux of warmer air up or down to that region. Lower in the ML warming is from the thermals or plumes originating at the surface. These plumes become cooler than the horizontal average in the EL where upper stability above the inversion interface causes them to turn downward. Here there are accompanying downward moving pockets of warm air associated with the upward moving plumes. All of this was seen in the visual aids presented by Sullivan et al. in [14].

In [8] Mahrt and Paumier examined the joint distributions of w' and θ' from measurements taken of mixed layers developed in the flow of cold air masses over a warm current. Their two dimensional representations clearly show the four quadrants: upward warm, upward cool, downward cool and downward warm.

Sorbjan in [10] asserted and demonstrated that the moments involving θ' particularly in the upper ML and EL are strongly influenced by the upper lapse rate γ . Whereas moments of w' were less so. These effects were seen when the corresponding vertical profiles were scaled by the convective scales (θ^* and w^*).

Bearing the above three studies in mind we separate the $w'\theta'$ into the four

quadrants and plot the average vertical scaled profiles as well as the 2d histograms at h and the EL limits. We can confirm that the upper extrema of the four individual quadrants exceed that of the average and are higher i.e. close to h (Figure 2.16). Higher stability results in a more pronounced peak particularly in the upward cool quadrant profile which corresponds to increased damping and a sharper decrease in velocity. Since warming in this region is associated with downward movement of air from above, the downward warm quadrant is important.

The 2d histograms at each level show increased spread of both θ' and w' with increased $\overline{w'\theta'_s}$ (Figures 2.18, ??, 2.19). There is damping of w' with increased γ . To isolate the effects of increased γ we should scale by the convective scales (θ^* and w^*) .

3.6 h and Δh based on Average Profiles

3.6.1 Reminder of Relevant Definitions

Our heights are defined based on the average vertical temperature gradient the principle length scale being h the vertical location of the maximum. Flux based heights are scaled by h to enable comparison with the frameworks of other studies.

3.6.2 $\frac{w_e}{w^*}$ vs Ri^{-1}

In Figure 2.22 h shows a $\frac{1}{2}$ power law relationship to time indicating we are in the regime outlined by Federovich et al. in [4]. Self similarity of the scaled heat flux profiles vs scaled height in Figure 2.4 indicate a more or less constant entrainment ratio, but also a more or less constant scaled entrainment depth with respect to time. Our Richardson numbers (Ris) increase with respect to time and again grouping according to γ is evident (Figure 2.24).

Kato and Philips successfully related the scaled entrainment rate of penetrative shear driven turbulence in their water-tank experiment in [7] to a

dimensionless group formed from the three main characteristics of the flow : the buoyancy jump across the interface, the turbulent velocity of the ML and the depth of the ML. IE

$$\frac{u_e}{u^*} \propto \frac{\rho_0 u^{*2}}{g \delta \rho D} \quad (3.3)$$

J. W. Deardorff and Stockton related their scaled entrainment of penetrative convection to this dimensionless group, substituting the shear driven velocity scale for the convective one, thus forming the now commonly used Richardson number (Ri) for the CBL. Their heights were determined from the vertical heat flux profiles. The heat flux profiles in turn were derived from two successive potential temperature profiles. The resulting relationship between scaled entrainment rate and Ri appears to potentially exhibit both -1 and $-\frac{3}{2}$ power laws.

Sullivan et al.'s data in [14] showed some scatter and they speculated that a power law other than -1 may have described the relationship at Ris smaller than 14. They compare the data to this fit:

$$\frac{w_e}{w^*} = 0.2 Ri^{-1} \quad (3.4)$$

Turner in [15] attribute the $-\frac{3}{2}$ power law to mixing that depends on the recoil of impinging eddies. Whereas Federovich et al. in [4] derive it from a best fit approximation of the Ri calculated using the buoyancy jump across the EL to scaled time (after $tN > 100$) and applying the zero order model relationship.

Brooks and Fowler's plot in [2] has relatively little scatter and exhibits a linear relationship (-1 power law) whereas Garcia and Mellado's data in [5] seems asymptotic to a linear relationship.

Our data based on the temperature jump across the entire EL shows a seemingly linear relationship (Figure 2.25).

3.6.3 $\frac{\Delta h}{h}$ vs Ri^{-1}

The EL tops as defined by the point at which the temperature gradient resumes γ seem to be scaled well by h (Figure 2.26). This seems in contrast to the assertion of Garcia and Mellado in [5] about the upper EL i.e. that length and buoyancy in this region are not scaled by the the CBL convective scales. The EL top as defined where the point at which the buoyancy flux decreases to close to zero, when scaled by h is comparable, but has greater scatter (Figure 2.27). But in both cases, the top limit is about $1.15 \times h$, and there is a barely perceptible, possible negative trend.

The scaled lower EL limits based on the increase in potential temperature gradient from zero, show a clearer increase but don't show the same kind of collapse across runs as the upper limit does (Figure 2.26). The scaled lower limit based on the flux profiles however, do collapse well (Figure 2.27). So we could say with some confidence that $\frac{h-z_{f0}}{h} \approx .2$ and this is comparable to Garcia and Mellado's lower EL sublayer.

So the scaled EL as defined by the vertical gradient in the potential temperature profile certainly decreases with respect to time. The scaled EL based on the flux profiles shows slight or no change with respect to time. This is in line to the findings of Brooks and Fowler in [2] even though their definition is slightly different IE $2 \times (z_f - z_{f0})$. But it is in stark contrast to what Federovich et al. show in [4] i.e. $\frac{z_{f1}-z_{f0}}{z_f}$ decreasing from about .6 to about 0.1. This could in part be explained by the difference in vertical resolution since according to Sullivan and Patton in [13] the shape of average heat flux profile in the EL is sensitive to grid size.

Sorbjan in [10] and [11] demonstrates how the surface and lower ML portions of the temperature gradient profile is scaled well by the convective scales but γ becomes more important in the EL. From our potential temperature profiles in Figure 2.7 we see that both γ and $\overline{w'\theta'}_s$ influence the warming of the ML. So this should reflect in particular in the downward flux

of warm air from the inversion IE at h . That is, increasing γ seems to result in an increased slightly positive gradient in the upper ML and this should relate to an increase in the downward flux warm air above it, for example at h .

So, first we define the EL lower limit as the point at which the vertical gradient exceeds a positive threshold that's less than γ and the same for all runs, at all times. We try three different values and note that there is a seeming decrease in the scaled magnitude with respect to Ri, bearing in mind the definition of the EL is included in the calculation of $\Delta\theta$ for Ri . Grouping according to γ is evident.

Scaling the vertical potential temperature gradient profiles by γ results in collapse to more or less one curve. The gradient profiles seem to show an increase in the peak gradient as the EL seems to narrow. This trend is apparent with respect to time and across runs. This portion of the profile has been scaled effectively by Sorbjan in [11] using $\frac{\Delta\theta}{\Delta h}$ and Garcia and Mellado using their buoyancy scale $b \approx N^2\delta + [\overline{b_0}(h) - \overline{b}(h)]$ where $\delta \propto \frac{w^*}{N}$ is their length-scale for the upper EL sublayer. Related to $\frac{\Delta\theta}{\Delta h}$ is the entrainment layer stratification parameter $G = \gamma \frac{\Delta h}{\Delta\theta}$ which Federovich et al. found to be constant throughout the quasi-steady state regime IE, $\Delta\theta \propto \Delta h$. This seems to contradict the apparent increase in maximum gradient with decrease in EL depth.

Bibliography

- [1] I. M. Brooks. Finding boundary layer height: Application of a wavelet covariance transform to lidar backscatter profiles. *Journal of Atmospheric and Ocean Technology*, 20:1194 – 1205, 2003. → pages
- [2] I. M. Brooks and A. M. Fowler. An evaluation of boundary-layer depth, inversion and entrainment parameters by large-eddy simulation. *Boundary-Layer Meteorology*, 142:245–263, 2012. → pages
- [3] J. W. Deardorff. Prediction of convective mixed-layer entrainment for realistic capping inversion structure. *Journal of the Atmospheric Sciences*, 36:424–436, 1979. → pages
- [4] E. Federovich, R. Conzemus, and D. Mironov. Convective entrainment into a shear-free, linearly stratified atmosphere: Bulk models reevaluated through large eddy simulation. *Journal of the Atmospheric Sciences*, 61:281 – 295, 2004. → pages
- [5] J. R. Garcia and J. P. Mellado. The two-layer structure of the entrainment zone in the convective boundary layer. *Journal of the Atmospheric Sciences*, 2014. doi:10.1175/JAS-D-130148.1. → pages
- [6] G. E. W. J. W. Deardorff and B. J. Stockton. Laboratory studies of the entrainment zone of a convectively mixed layer. *J. Fluid Mech.*, 100:41–64, 1980. → pages
- [7] H. Kato and O. M. Philips. On the penetration of a turbulent layer into stratified fluid. *J. Fluid Mech.*, 37:644–655, 1969. → pages
- [8] L. Mahrt and J. Paumier. Heat transport in the atmospheric boundary layer. *Journal of the Atmospheric Sciences*, 41:3061–3075, 1984. → pages

- [9] H. Schmidt and U. Schumann. Coherent structure of the convective boundary layer derived from larg-eddy simulations. *J. Fluid. Mech.*, 200:511–562, 1989. → pages
- [10] Z. Sorbjan. Effects caused by varying the strenth of the capping inversion based on a large eddie simulation of the shear free convective boundary layer. *Journal of the Atmospheric Sciences*, 53:2015 – 2023, 1996. → pages
- [11] Z. Sorbjan. Similarity of scalar fields in the convective boundary layer. *Journal of the Atmospheric Sciences*, 56:2212 – 2221, 1999. → pages
- [12] D. G. Steyn, M. Baldi, and R. M. Hoff. The detection of mixed layer depth and entrainment zone thickness from lidar backscatter profiles. *Journal of Atmospheric and Oceanic Technology*, 16:953–959, 1999. → pages
- [13] P. P. Sullivan and E. G. Patton. The effect of mesh resolution on convective boundary layer statistics and structures generated by large eddie simulation. *Journal of the Atmospheric Sciences*, 58:2395–2415, 2011. doi:10.1175/JAS-D-10-05010.1. → pages
- [14] P. P. Sullivan, C.-H. Moeng, B. Stevens, D. H. Lenschow, and S. D. Mayor. Structure of the entrainment zone capping the convective atmospheric boundary layer. *Journal of the Atmospheric Sciences*, 55:3042–3063, 1998. doi:10.1007/s10546-011-9668-3. → pages
- [15] J. S. Turner. Turbulent entrainment: the development of the entrainment assumption and its application to geophysical flows. *J. Fluid Mech.*, 173:431–471, 1986. → pages
- [16] E. Vieth. Fitting piecewise linear regression functions to biological responses. *Journal of Applied Physiology*, 67:390–396, 2011. → pages